

The impact of Radial and Quasi-Radial IMF on the Earth's Magnetopause Size and Shape, and Dawn-Dusk Asymmetry from Global 3D Kinetic Simulations

Suleiman M Baraka^{1,3}, O. Le Contel², L. Ben-Jaffel³, W. B. Moore^{1,4}

¹National Institute of Aerospace, 100 Exploration Way, Hampton, VA 23666

²Laboratoire de Physique des Plasmas, UMR7648 ,CNRS/Ecole Polytechnique Institut Polytechnique de Paris/Sorbonne Université/Université Paris-Saclay/Observatoire de Paris, Paris, France.

³Institut d'Astrophysique de Paris, UMR7095, Sorbonne Université, Paris, France

⁴Hampton University, 154 William R. Harvey Way Hampton, VA 23668

Key Points:

- Magnetosphere.
- IMF Radial and Quasi Radial Orientations.
- Solar Wind.
- Temperature anisotropy and velocity distribution function.
- IAPIC Kinetic Electromagnetic Relativistic Particle Code.

Abstract

The boundary between the solar wind (SW) and the Earth's magnetosphere, named the magnetopause (MP), is highly dynamic. Its location and shape can vary as a function of different SW parameters such as density, velocity, and interplanetary magnetic field (IMF) orientations. In the present paper an event of July 26, 2017, captured by THEMIS spacecraft is simulated by a 3D kinetic Particle-In-Cell (IAPIC) code. We investigate the impact of radial ($B = B_x$) and quasi-radial ($B_z < B_x, B_y$) IMF on the shape and size of Earth's MP for a dipole tilt of 31° using both maximum density steepening and pressure system balance methods for identifying the boundary. We found that, compared with northward or southward-dominant IMF conditions, the MP position expands asymmetrically by 8 to 22% under radial IMF. In addition, we construct the MP shape along the tilted magnetic equator and the OX axes showing that the expansion is asymmetric, not global, stronger on the MP flanks, and is sensitive to the ambient IMF. Finally, we investigate the contribution of SW ions back-scattered by the bow shock to the MP expansion, the temperature anisotropy in the magnetosheath, and a strong dawn-dusk asymmetry in MP location. These simulations can substantially contribute in a complementary manner with the available MHD and Hybrid models to both future space mission measurements and exoplanet magnetosphere investigations.

Plain Language Summary The Earth magnetopause (MP) is a sensitive region where the pressure of the Earth magnetic field balances the shocked solar wind ram and thermal pressures. Accurate space weather monitoring and forecast require an in-depth knowledge of that region and of the physical processes that affect it. In that frame, we started to investigate kinetic first-order effects on the MP size, location, and shape by using IAPIC, a fully global 3D PIC code. Since the space age, in late 1950s, huge efforts had been invested for modeling the solar wind magnetosphere-ionosphere-magnetosheath coupling. In a complementary manner with the existing MHD, and hybrid models, we used IAPIC to investigate the impact of radial IMF on MP shape, size and location. We are able to

44 extract the shape and location of the MP in two key planes, namely the tilted magnetic
45 equator and the GSM equatorial plane that contains the Earth-Sun line. This allows us to
46 accurately estimate the sensitivity of the MP to the ambient IMF, particularly the role of
47 the less-studied population of SW species backscattered by the Earth bow shock.

1 Introduction

The magnetic fields of planets such as Mercury, Earth, and the giant planets present an obstacle to the supersonic solar wind (SW). As a result, a shock forms and the solar wind is redirected around the obstacle producing a cavity which is called the magnetosphere (e.g., Parks, 1991). The boundary between the solar wind and the plasma in the magnetosphere is the magnetopause (MP). At the subsolar point, the classical fluid description of the solar wind stagnation flow derives the location of the magnetopause by the balance between the planetary magnetic field pressure and the dynamic pressure of the SW. Plasma boundary layers form on either side of the magnetopause with the magnetosheath boundary layer (MSBL) on the sunward side and the low-latitude boundary layer (LLBL) on the magnetosphere side. Both layers play an important role in plasma exchange across the magnetopause (e.g., Pi et al., 2018).

The magnetopause structure is significantly influenced by the interplanetary magnetic field (IMF) orientation. While the impact of southward (Yu & Ridley, 2009; Heikkila, 2011; Tan et al., 2011; A. Suvorova & Dmitriev, 2015; Berchem et al., 2016) and northward IMF (Sorathia et al., 2019; Luo et al., 2013; Bobra et al., 2004; J. Wang et al., 2018) on the dynamics of Earth's magnetosphere have been extensively studied in the last four decades, only recently has attention been focused on radially-dominant IMF conditions, which will be called radial IMF for the remainder of this paper. For most solar wind plasma conditions at the orbital position of planets, bow shocks are collisionless and supercritical shocks, which by definition, reflect and accelerate a fraction of the plasma impinging on them. These backstreaming particles lead to the formation of the ion foreshock region upstream (e.g., Turner et al., 2018, p. 206). A theoretical treatment of microscopic properties of the magnetopause is thoroughly discussed in (Spreiter & Alksne, 1969; Willis, 1978, and references therein). Additionally, Treumann (2009) discussed the non-relativistic collisionless shocks, bow shocks and magnetopause dynamical process.

Following early satellite observations (Greenstadt et al., 1968; Asbridge et al., 1968), the idea of an extended foreshock that diverts the solar wind around the magnetosphere and reduces the solar wind dynamic pressure at the subsolar magnetopause was proposed for radial IMF conditions (Fairfield et al., 1990; Merka et al., 2003; Jelínek et al., 2010; A. V. Suvorova et al., 2010). The distance and shape of the equatorial magnetopause is strongly affected by radial IMF, resulting in a global expansion of the magnetopause (Grygorov et al., 2017). Zhang et al. (2019) found that a dawn-dusk asymmetry exists in the magnetosheath, directly related to the IMF orientation. Evidently, the plasma distribution and the IMF are correlated to these asymmetries. Additionally, these asymmetries are either generated at the bow shock or inside the magnetosheath itself.

Most magnetopause observations during radial IMF have noted a large magnetopause expansion that was connected with a significant distortion of the magnetopause surface. Large magnetopause distortion and anomalous sunward magnetosheath flows were reported in one radial IMF event by (Shue et al., 2009). The finding of magnetopause displacement during nearly radial IMF conditions was also documented in a statistical study based on a large set of magnetopause crossings using GEOS (Dušík et al., 2010). A systematic increase of observed magnetopause distances for radial IMF was found, ranging from $0.3R_E$ at 90° cone angle to $\approx 1.7R_E$ at 0° or 180° cone angles compared to empirical models. In contrast, using THEMIS data and empirical models of the MP, Grygorov et al. (2017) concluded that the distance of the equatorial magnetopause is strongly affected by radial IMF, expanding globally and independent of the local time, upstream value of other solar wind parameters or the tilt of the Earth magnetic dipole.

It is interesting to remark that no self-consistent model exists today in the literature that can explain the observed magnetopause displacement or its asymmetry, particularly with the difficulty MHD approaches have to accurately model reflected solar wind ions in the foreshock region (Sibeck et al., 2001). In a recent study, A. Samsonov et al. (2017) used previous statistical results to suggest that the density and velocity in the foreshock region

decrease to $\sim 60\%$ and $\sim 94\%$ of the undisturbed solar wind values when the cone angle falls below 50° causing a drop in the solar wind dynamic pressure of $\sim 53\%$ that might cause the magnetopause displacement. In a second step, those authors modified the upstream solar wind parameters in a global MHD model to take these foreshock effects into account, which helped them predict magnetopause distances during radial IMF intervals close to those observed by THEMIS. According to A. Samsonov et al. (2017), the strong total pressure decrease in the data seems to be a local, rather than a global, phenomenon. Those authors conceded that their model was not self-consistent in the sense that the modified upstream solar wind parameter model was global and not specific to the foreshock region for which the statistical results were initially derived.

In addition to the expansion of the MP, the other focus of this study is the generation of dawn-dusk asymmetry under radial IMF, which has been investigated for many decades (Akasofu et al., 1982; Akasofu, 1991; Haaland et al., 2017, and references therein). Dawn-dusk asymmetries are ubiquitous features of the coupled solar wind-magnetosphere-Ionosphere system. During the last decades, increasing availability of satellite and ground-based measurements has made it possible to study these phenomena in more detail (e.g., B. M. Walsh, 2017). Most studies reported so far agree that the dawn-dusk asymmetry is primarily the result of the Parker spiral solar wind impinging with a specific geometric configuration that impacts and preconditions the magnetosphere (e.g., Haaland et al., 2017, and references therein). In radial IMF predominant conditions, one would then expect a quasi-symmetric configuration of the magnetosphere in which the Parker spiral effect would cease and other physical processes, like kinetic effects, would drive any dawn-dusk asymmetry. For instance, statistical studies based on THEMIS and Cluster measurements confirm a rather global expansion of the magnetopause under radial IMF without significant dawn-dusk asymmetries detected (Zhang et al., 2019). The same statistical study showed that magnetic reconnection (MR) is nearly absent during radial IMF, in contrast to the north IMF conditions during which MR and the consequent dawn-dusk asymmetries are strong (Zhang et al., 2019).

Kinetic effects are expected to trigger a large set of distinct dawn-dusk asymmetries upstream of the magnetosphere due to the formation of the foreshock region that is connected with solar wind population backscattered by the bow shock. Although much of the plasma passes through the bow shock, the reflected population generates a number of plasma instabilities, which trigger waves and generate wave particle interactions as well as other dynamics at the quasi-parallel shock that should favor dawn-dusk asymmetries (e.g., B. M. Walsh, 2017, and references therein for more details). The radial IMF condition would thus be the ideal configuration to reveal such kinetic effects and measure their weight in the dawn-dusk asymmetry so far observed (Zhang et al., 2019). For reference, using Cluster single/multiple spacecraft measurements, Haaland et al. (2014) discussed the dawn-dusk asymmetry at the flanks and at the dayside MP. Similar results were also reported by Haaland et al. (2019), as observed by two of the THEMIS spacecraft, showing the magnetopause being thicker on dawn ($\sim 14\lambda_i$, λ_i being the ion inertial length) than on dusk ($\sim 8\lambda_i$), yet no radial IMF conditions were covered in the statistical study. Additionally, other observations from INTERBALL-1 and MAGION-4 spacecraft revealed asymmetry and deformation at the turbulent magnetopause (Šafránková et al., 2000). From Geotail observations for northern and southern IMF, C.-P. Wang et al. (2006) thoroughly discussed the dawn-dusk asymmetry in ion density and temperature based on equatorial distribution of plasma sheet ions.

To interpret the magnetopause motion and the dawn-dusk asymmetry, many sophisticated models have been proposed in the past, ranging from MHD to hybrid simulations. Early theoretical studies showed a contrast of 10%-20% between dawn and dusk bulk plasma properties density, velocity, etc (e.g., Němeček et al., 2002; B. M. Walsh et al., 2012). However, those MHD-based models do not handle kinetic effects, particularly at the foreshock region. For instance, using a global hybrid model (kinetic ions and fluid electrons), Blanco-Cano et al. (2009a) studied radial IMF ($\theta_{vB} = 0$) impact on the solar wind interaction with the Earth's magnetosphere. The study focused on the micro-physics processes and wave-particle interactions in the foreshock region but briefly mentioned the dawn-dusk asymmetry

issue. Three other models i.e. hybrid, Hall-less and Hall-MHD simulations have been tested in one study by Karimabadi et al. (2004) for the analysis of MR regimes with the conclusion that dawn-dusk asymmetry is obtained and should be related to ions flow. Recently, Turc et al. (2020) used the hybrid -Vlasiator 2D-3V code to study asymmetries in the Earth magnetosheath for different IMF conditions. For reference, the code provides a kinetic description of ions, solving directly the Vlasov equation for the particles distribution function in 2D-3D space, but assumes a fluid description for electron (e.g. Palmroth et al., 2018). The authors report asymmetries larger than observed for the magnetic field strength, the plasma density, and bulk velocity, a discrepancy that was attributed to using a single set of upstream conditions in their simulations. It is interesting to remark that those authors obtained a stronger asymmetry for magnetic field strength when IMF gets closer to the radial configuration. However, it was not clear how the 2D spatial assumption and the fluid description of electrons in their simulations affected the reported magnetosheath asymmetries.

Based on the discussion above, two important questions appear: 1) what happens to the magnetopause shape, size, and location if flow-aligned IMF is applied to the system when kinetic effects are included for all species? and 2) does this generate asymmetry in dawn-dusk and south-north direction in the dayside magnetosphere?

To answer these questions, we undertake a modeling study utilizing IAPIC, a particles-in-cell code (discussed in section 2). Our strategy is to be able to follow ions and electrons self-consistently with the Maxwell equations describing the fields. Thus the full range of collisionless plasma physics is captured for the macro-ions and macro-electrons involved in IAPIC, yet with limitations due to the grid spatial resolution and assumptions made on the plasma properties (particles density, ion/electron mass ratio, etc.) that we carefully discuss in section 2 (see Blanco-Cano et al., 2006; Eastwood, 2008; Jacobsen et al., 2009; Brackbill, 2011; Masters et al., 2013; Ben-Jaffel & Ballester, 2014; S. Baraka, 2016). We adopt the initial and the boundary conditions reported in (A. V. Suvorova et al., 2010; A. Samsonov et al., 2017).

This paper is structured as follows. This section has introduced the impact of radial IMF orientation on the dynamics of the Earth's magnetosphere and presented a brief survey of observations of asymmetry in planetary magnetospheres. Two IMF orientations, namely, radial IMF ($\mathbf{B} = \mathbf{B}_x$) and quasi-radial IMF ($B_x \text{ \& } B_y > B_z$) will be covered in the current study. In section 2, an introduction to the development of IAPIC code in addition to the code description and the scaling of plasma parameters is presented. In section 4, our findings regarding the magnetopause motion and the magnetosheath asymmetry will be shown. Results will be compared to previous modeling results and observations. In section 6, we present a thorough discussion about what purely and quasi-radial IMF impact on the dynamics of the Earth's magnetosphere on light of the results obtained so far.

2 Initial conditions and Simulation Model: IAPIC

2.1 Simulation Model: IAPIC

We use Institut d’Astrophysique de Paris-Particle-In-Cell EM 3D global code (IAPIC) for treating the plasma kinetically, previously applied to simulate various magnetospheres in the solar system (S. Baraka & Ben-Jaffel, 2011; Ben-Jaffel & Ballester, 2013, 2014; S. Baraka, 2016). IAPIC handles the equations of motion for large number of macro-particles (macro-ions and macro-electrons) self-consistently under the direct impact of electromagnetic fields through Lorentz force law (S. Baraka & Ben-Jaffel, 2007; Artemyev & Zelenyi, 2012).

The code was originally written by (Buneman et al., 1992) which used the boundary conditions reported in (Lindman, 1975) and charge conserving conditions as described in (Villasenor & Buneman, 1992). We adopt the initial conditions reported in (A. Samsonov et al., 2017) and scaled them to IAPIC values using a transformation matrix to convert GSM coordinates to the IAPIC code coordinates (see Fig. 1) as reported in (Cai et al., 2003). The solar wind parameters are normalized to spatial and temporal parameters and tabulated in Table 1 for radial IMF and Table 2 for quasi radial IMF (Table 1. Cai et al., 2015).

We follow the evolution of the macrostructure magnetosphere and chose time step $\Delta t = 3700$ as our comparison point. Each step time is equivalent to ≈ 0.38 sec. The spatial resolution of the code is $0.2R_E$ loaded with 70×10^6 pair particles, with an ion to electron mass ratio of 64.

Here we tabulate our normalized solar wind parameters to temporal and spatial values for both IMF orientations(i.e. Tables 1 & 2). The parameters are set such that a consistent initial conditions are validated before the code run starts, denoted as $\Delta t = 0$, and at the step time, where the current study is considered i.e. $\Delta t = 3700$. These two tables are compared to similar study by (Cai et al., 2015, e.g. Table 1)

Step time		$\Delta t = 0$		$\Delta t = 3700$	
Species/Parameters	Normalization	ions	electrons	ions	electrons
Thermal velocity, $V_{thi,e}$	$\tilde{v}_{thi,e} = \frac{v_{thi,e}}{\Delta/\Delta t}$	0.177	0.708	0.135	1.069
Debye length, $\Delta_{i,e}$	$\tilde{\lambda}_{i,e} = \frac{v_{thi,e}}{\omega_{pi,e}}$	0.8	0.4	0.52	0.52
Larmor radius, $\lambda_{i,e}$	$\tilde{\rho}_{ci,e} = \frac{\tilde{v}_{thi,e}}{\tilde{\omega}_{ci,e}}$	8.85	0.49	45	2.6
Gyro-frequency $\omega_{ci,e}$	$\tilde{\omega}_{ci,e} = \omega_{ci,e} \cdot \Delta t$	0.02	1.425	0.003	0.41
Plasma-frequency $\omega_{pi,e}$	$\tilde{\omega}_{pi,e} = \omega_{pi,e} \cdot \Delta t$	0.22	1.77	0.27	2.14
Temperature, $T_{i,e}$	$\tilde{T}_e = 2\tilde{v}_{the}^2, \tilde{T}_i = 2\tilde{v}_{thi}^2 \frac{m_i}{m_e}$	4.	1.	2.33	2.28
Gyroperiod	$\tilde{\tau}_{ci,e} = \frac{2\pi}{\tilde{\omega}_{ci,e}}$	314.15	4.4	2094.34	15.32
Inertial length $d_{i,e}$	$\tilde{d}_{i,e} = \frac{\tilde{c}}{\tilde{\omega}_{pi,e}}$	2.27	2.82	1.89	0.23

Unitless values		
Step time	$\Delta t = 0$	$\Delta t = 3700$
Sound speed C_s	0.045	0.050
Alfvén speed v_A	0.050	0.012
Alfvén Mach number M_A	2.83	5.4351
Sonic Mach number M_s	3.16	1.3
Magnetosonic Mach number M_{ms}	2.0	1.27

Loaded Simulation Box Information		
grid size		$\Delta = 0.2R_E = \Delta x = \Delta y = \Delta z$
Time Step		$\Delta t = \Delta_x/\Delta_v = 1.416$
Simulation box size		$(305 \times 225 \times 255)\Delta$
# of pair-particles		7×10^7 ion/electrons pairs
Ion to electron mass ratio		64
Particle density		$n_i = n_e = 4/\Delta^3$

Table 1. Normalized solar wind parameters at the initial state and after 3700 Δt in the solar wind for both ions and electrons for radial IMF.

Step time		$\Delta t = 0$		$\Delta t = 3700$	
Species/Parameters	Normalization	ions	electrons	ions	electrons
Thermal velocity, $V_{thi,e}$	$\tilde{v}_{thi,e} = \frac{v_{i,e}}{\Delta/\Delta t}$	0.177	0.708	0.127	1.027
Debye length, $\lambda_{Di,e}$	$\tilde{\lambda}_{i,e} = \frac{v_{thi,e}}{\omega_{pi,e}}$	0.8	0.4	0.529	0.52
Larmor radius, $\lambda_{i,e}$	$\tilde{\rho}_{ci,e} = \frac{\tilde{v}_{thi,e}}{\tilde{\omega}_{ci,e}}$	3.175	0.29	25.4	1.95
Gyro-frequency $\omega_{ci,e}$	$\tilde{\omega}_{ci,e} = \omega_{ci,e} \cdot \Delta t$	0.04	2.435	0.005	0.525
Plasma-frequency $\omega_{pi,e}$	$\tilde{\omega}_{pi,e} = \omega_{pi,e} \cdot \Delta t$	0.22	1.77	0.24	1.955
Temperature, $T_{i,e}$	$\tilde{T}_e = 2\tilde{v}_{the}^2, \tilde{T}_i = 2\tilde{v}_{thi}^2 \frac{m_i}{m_e}$	4.010	1.0	2.065	2.109
Gyroperiod	$\tilde{\tau}_{ci,e} = \frac{2\pi}{\tilde{\omega}_{ci,e}}$	157.27	2.58	1256.63	11.960
Inertial length $d_{i,e}$	$\tilde{d}_{i,e} = \frac{\tilde{c}}{\tilde{\omega}_{pi,e}}$	2.27	0.282	2.08	0.255
Unitless values					
Step time	1			3700	
Sound speed C_s	0.04			0.035	
Alfvén speed v_A	0.085			0.017	
Alfvén Mach number M_A	1.65			2.855	
Sonic Mach number M_s	3.16			1.424	
Magnetosonic Mach number M_{ms}	1.463			1.272	
Loaded Simulation Box Information					
grid size		$\Delta = 0.2R_E = \Delta x = \Delta y = \Delta z$			
Time Step		$\Delta t = \Delta_x/\Delta_v = 1.416$			
Simulation box size		$(305 \times 225 \times 255)\Delta$			
# of pair-particles		7×10^7 ion/electrons pairs			
Ion to electron mass ratio		64			
Particle density		$n_i = n_e = 4/\Delta^3$			

Table 2. Normalized solar wind parameters at the initial state and after 3700 Δt in the solar wind for both ions and electrons for quasi-radial IMF.

2.2 Initial conditions

In IAPIC, the spatial and temporal scales are chosen in such a way to scale macroparticles properties (mass ratio and charge to mass ratio, etc ...) in order to be able to regenerate MHD large-scale classical structure of the Earth's magnetosphere (e. g., Omid et al., 2004). For their modeling, A. Samsonov et al. (2017) used MHD and Community Coordinated Modeling Center (CCMC) resources, while the observational data are obtained from ACE, THEMIS and WIND spacecraft. Samsonov et al. studied the impact of quasi radial IMF on the magnetopause size and shape. Contextually, in the current study, we used their MHD initial conditions and scaled them to the IAPIC initial condition values not only for quasi-radial IMF (where B_x and B_y are dominant over B_z), but for purely radial IMF as well (where B_y and B_z are absent). The radial IMF is an additional case included to study the differences and similarities of the radial nature of IMF on both magnetopause shape and size and their role in creating the asymmetry in dawn-dusk direction. The initial conditions of A. Samsonov et al. (2017) and our two IMF orientations are then tabulated in Table 3.

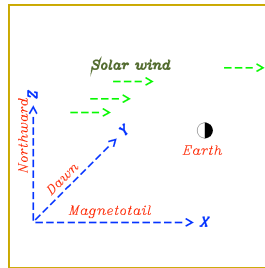


Figure 1. Orientation reference of the code inside the simulation box in 3D (Cai et al., 2003)

Table 3. MHD initial conditions and their corresponding IAPIC scaled values for radial and quasi-radial IMF orientation(A. Samsonov et al., 2017).

Parameters	MHD	IAPIC _{radial}	IAPIC _{quasi-radial}
T_{sw} Kelvin	32263	5×10^4	5×10^4
V_x km/s	-470.69	0.1412	0.1412
V_y km/s	-7.80	0	0
V_z km/s	-5.0909	0	0
IMF _{x} nT	-2.2	0.25	0.25
IMF _{y} nT	2.99	0	-0.34
IMF _{z} nT	0.659	0	0.075
Tilt angle	31°	31°	31°

3 Simulation Results

To our knowledge, a full 3D global kinetic modeling of radial IMF impacts on the dynamics of the magnetosphere has not been published, though the backstreaming of ions in the solar wind flow has been theoretically discussed (e.g., Willis, 1978, Eq. 3). The quasi-radial IMF event on July, 16th, 2007 observed by the THEMIS probes was chosen because it has been the subject of several detailed studies (Jelínek et al., 2010; A. V. Suvorova et al., 2010; A. Samsonov et al., 2017). The solar wind parameters and initial cond

4 Simulation Results

To our knowledge, a full 3D global kinetic modeling of radial IMF impacts on the dynamics of the magnetosphere has not been published, though the backstreaming of ions in the solar wind flow has been theoretically discussed (e.g., Willis, 1978, Eq. 3). The quasi-radial IMF event on July, 16th, 2007 observed by the THEMIS probes was chosen because it has been the subject of several detailed studies (Jelínek et al., 2010; A. V. Suvorova et al., 2010; A. Samsonov et al., 2017). The solar wind parameters and initial conditions were scaled for IAPIC as described in section 2. For purposes of comparison, we discuss

in detail the plasma properties at the time step $3700\Delta t$ of our simulation for both full and quasi-radial IMF. This time step corresponds to ≈ 24 minutes of real time (based on scaled data relative to spatial and temporal resolution of the code), a relatively long enough period to perform kinetic simulation of the problem in hand. In the following, IAPIC simulation results are analyzed to determine the magnetopause shape, size and location for the two IMF conditions assumed, which give us a good frame to characterize any dawn-dusk asymmetry in the system.

4.1 Magnetopause response to the full and quasi-radial IMF

We derive the magnetopause size using the steepening of the maximum radial density gradient (e.g., Garcia & Hughes, 2007; J. Lu et al., 2015). Because of the magnetic field axis tilt (31°), the system is inherently asymmetric and the Cartesian grid used in the IAPIC simulations is not adequate to accurately derive a density gradient in most planes, particularly in the magnetic equatorial plane. To overcome this difficulty, we transform our Cartesian 3D simulation box quantities (density, velocity vector, etc. at (x,y,z) positions) into a spherical 3D domain (same quantities at (r, θ, ϕ) positions), at the price of losing data from regions outside a spherical volume of radius equal to the smallest dimension of the initial Cartesian box (OY or OZ in our case). Our study does not suffer of that limitation because the dayside MP, our region of interest, is located inside the selected spherical domain. After checking that both reference frames provide the same spatial distribution of all physical quantities along OX, OY, and OZ axis, we focus on deriving the magnetopause size at two key planes, namely the magnetic equatorial plane $\theta = -31^\circ$ and the plane $\theta = 0^\circ$ that contains the Sun-Earth line.

In a first step, we focus on the direction defined by $\phi = -180^\circ$ in both planes. We derive comparable values for the magnetopause position at $\sim 10.4, \sim 11.0$) R_E respectively for radial and quasi-radial IMF along Sun-Earth axis and equal to $(\sim 10.4, \sim 10.7)$ R_E when the effect of backstreaming ions is removed. However, along the tilted axis contained in the magnetic equatorial plane, the magnetopause positions are $(10.5, 11.8)$ R_E with bulk

flow and equal to $10.8, 11.8 R_E$ without backstreaming ions, respectively for the two IMF conditions.

First, we note that the different magnetopause positions derived from the IAPIC simulation are all larger than the expected magnetopause position ($\sim 9.6 R_E$) derived from the classical $1/6$ power law corresponding to the initial solar wind parameters used in our simulations. All values derived show an expansion of the magnetopause position along the two selected axes but also sunward, as if the magnetopause is subject to a reduced SW pressure that allows the dipole magnetic field network to expand outward. It is remarkable that our model predicts the magnetopause expansion in the range $(1.4-2.2) R_E$ along Sun-Earth axis and Magnetic equator axis for quasi-radial IMF. This expansion range is consistent with MHD simulations and THEMIS observations shown by A. Samsonov et al. (2017) which reported magnetopause expansion in the range $(1.3-1.5) R_E$. On the other hand and for purely radial IMF along the two axes, the magnetopause expands in the range $(0.8-0.9) R_E$ and therefore smaller than in the quasi-radial case.

In the following, we explore our (3D, 3V) IAPIC simulation results to try uncover potential processes that could be at the origin of the measured expansion. Since early reports on the expansion of the MP, several studies pointed to the potential impact of kinetic effects, particularly with the detection of the signature of particles streaming in a direction opposite to the solar wind (Spreiter & Alksne, 1969; Willis, 1978, 1978; Sibeck et al., 2001; A. Samsonov et al., 2017). As IAPIC simulations offer the access to all populations of particles (macro-particles) with specific kinetic properties, we tried to extract those particles on the dayside that move sunward, against the main impinging solar flow. That statistical sub-population of particles has its own kinetic properties and most importantly counter-balances the ram pressure of the incident solar flow, as if it was originating from the magnetosphere and flowing outward. It is important to stress that this population has kinetic properties (temperature, speed, etc) much different from the planetary ionospheric population that flows from the plasmasphere or the polar wind. In Fig. 2, bulk pressures (dynamic, thermal

Maximum Density Steepening magnetopause derivation				
IMF /Axis	Sun-Earth Axis		Tilted Magnetic equator axis	
Kinetic effects	Yes	No	Yes	No
magnetopause for radial IMF	10.4 R_E	10.4 R_E	10.5 R_E	10.8 R_E
magnetopause for quasi radial	11.0 R_E	10.7 R_E	11.8 R_E	11.8 R_E
Pressure balance magnetopause derivation				
IMF/Axis	Sun-Earth Axis		Tilted Magnetic equator axis	
Kinetic effects	Yes	No	Yes	No
magnetopause for radial IMF	10.5 R_E	9.7 R_E	11.2 R_E	10.8 R_E
magnetopause for quasi radial	11.2 R_E	10.8 R_E	11.7 R_E	11.1 R_E

Table 4. Summary of results: magnetopause is derived in two different methods. One relies on density gradient maximum steeping and the other for pressure balance downstream of the bow shock. Both methods are derived along Sun-Earth Axis and along Tilted Magnetic equator axes. Additionally, magnetopause is derived when backstreaming ions are included (kinetic effect) and without them. The slight difference of the measurements in both methods emphasize the impact of density alone and the velocity and thermal pressure on the other hand on the magnetopause derivation (e.g., A. Samsonov et al., 2020). As per IAPIC result, magnetopause reads $[10.4, 11.0] R_E$ and $[10.5, 11.2] R_E$ for radial and quasi-radial IMF when measured by the density and pressure methods respectively

denoted P_{dyn} and P_{thm} respectively) are co-plotted with and without backstreaming ions to visualize the difference they make in the pressure balance. P_{dyn} and P_{thm} encounter P_{mag} at two points, i.e. with and without backstreaming ions included. Kinetically, the magnetopause is derived with the pressure balance that includes bulk contents which revealed the size of the MP, as $10.5 R_E$ for radial IMF and $11.2 R_E$ for quasi-radial IMF along the Sun-Earth axis. In the magnetosheath the thermal pressure is dominant over dynamic pressure. Importantly, if the backstreaming ion effect is dropped, then there should be contraction of the magnetopause size, which reads the values of 9.7 and $10.8 R_E$ for same IMF orientations respectively. The magnetopause is also measured along the tilted magnetic equator axis with and without backstreaming ions and found equal to 11.2, $10.8 R_E$ for radial IMF and 11.7, $11.1 R_E$ for quasi-radial IMF, respectively. To summarize, these findings are tabulated in Table 7.

We report new results to track the magnetopause shape for both IMF orientations at two different locations namely along the Sun-Earth axis and along the tilted magnetic equator axis.

The equatorial plane is used to track the magnetopause shape using spherical coordinates ($\phi = -180^\circ$ at the dayside standoff distance) and ($\theta = 0$) along OX and ($\theta = -31$) along the magnetic equator axis of the tilted Earth's dipole field. We track the magnetopause shape every 20° along ϕ in two different manners (e.g., Fig. 3), using maximum density gradient as reported in Table 7. For instance, for the two IMF orientations, we first compare magnetopause shapes in Fig. 3A, B respectively along Sun-Earth and the tilted magnetic equator axes. In a second step, we compare magnetopause shapes for the same IMF orientation as in Fig. 3C and D. The only difference between the two IMF orientations is the large B_y domination in quasi-radial case (case study compared with A. Samsonov et al. (2017)). The impact of B_y is clearly depicted and results in squeezing the magnetopause shape at around $8R_E$ on the dawn side and at around $12R_E$ on the dusk side on Sun-Earth line (Fig. 3A). Furthermore, the magnetopause shape for radial IMF is more flared out and extended in the equatorial plane up to $15R_E$, but both shapes expanded along Sun-Earth line up to 10.4 and $10.98 R_E$, respectively. In Fig. 3B, the magnetopause shape is derived for both IMF orientations along the tilted magnetic axis. For radial IMF, it is more symmetric and more flared out than for quasi-radial IMF and the impact of B_y results in confining the global shape of the magnetopause along this direction. It is worth noting that in Fig. 3B, the part of the magnetopause in the dawn direction is more flattened because the plasma flow dynamic pressure in this direction is larger than in the dusk direction (see Fig. 4C, D and Fig. 6.)

In Fig. 3C, the magnetopause shape is compared for the same IMF direction but at two different locations i.e. along the Sun-Earth and the tilted magnetic equator axes. The difference between the two shapes appears in the dawn-side portion of the MP. For the quasi-radial IMF, the confinement of the magnetopause due to the B_y effect is stronger along the Sun-Earth direction than along the tilted magnetic equator axis. In order to check the magnetopause location from the linear density profile in 3D, we use IAPIC data to plot the solar wind plasma density for both ions and electrons (Fig. 6A, B) for the two IMF directions in three planes from -20 to $-10 R_E$ on OX, and -20 to $20R_E$ on OY, and OZ.

For the radial IMF, it is found that the inflow solar wind starts encountering the dipole field at the bow shock ($\approx 14R_E$). It is worth noting that the density should decrease to almost zero at the magnetopause position theoretically, but in our case there are still some plasma populations inside the magnetosphere along the Sun-Earth line, which is in agreement with experimental data (A. A. Samsonov & Pudovkin, 2000), additionally, it is practically difficult to account for perfect normal angle between incident solar wind and the magnetopause standoff boundary. Whilst, in Dusk-Dawn direction, the plasma boundary layer at $\pm 10R_E$ is asymmetric and is denser on the dusk side due to the effect of B_y . Furthermore, the structure in the South-North plane shows the two boundaries in asymmetric manner with the northern part having higher plasma density populations than the southern part.

On the other hand, for quasi-radial IMF, the linear density along OX has a double hump, tracking plasma inflow and the backstreaming ions/electrons, the plasma humagnetopause is seen at around $-16R_E$, and is apparently not due to backstreaming particles, and may be generated by wave-particle interactions (see Fig. 10, Fig. 8, and Fig. 9), this density humagnetopause did not appear in the radial IMF structure. The linear density along Dusk-Dawn shows the asymmetric boundary layer structure with higher density on the dawn side than on the dusk side while in the South-North direction the linear density shows a high peak of plasma of 1.5 times higher in the south region than in the northern one.

The other major components of the solar wind dynamics is its velocity modulus that is shown in Fig. 7 in the same order. To better visualize a large scale image of the system, contour plotting is conducted to show the plasma density distribution and magnetic field topology in 3D as in Fig. 4 & 5. It is found that the planet tilt (31°) has a major impact on the global macro-structure of the magnetosphere in the simulation box of size ($\approx 60 \times 40 \times 40 R_E$). In Fig. 4A, when the forefront of the solar wind coplanar inflow approaches the magnetosheath it hits the upper boundary of the magnetopause before the tilted magnetic equator axis, this makes plasma override the boundary there before it reaches the lower boundary. This results in squeezing the magnetopause at high latitude and relaxes it in lower latitude thus

making it flares out at around $20R_E$ (see also Fig. 3). There is around $6R_E$ vertical distance between the Sun-Earth and the tilted magnetic equator axes. Ionosphere is not included in the current study, as particles entry inside the magnetosphere is seen up to $5R_E$. The plasmasphere is shown up to $7R_E$. In Fig. 4B showing the plasma distribution for quasi-radial IMF, there is a plasma jumagnetopause (hump) of $\approx 2.3R_E$ thickness between -17 and -14.5 along the Sun-Earth line and extended curve-linearly from -12 (south) to 7 (north) in a dome-like shape. It is not clear what causes this humagnetopause that is absent in the radial IMF case at the same time step. The dynamic pressure at both cusps is relatively equivalent contrary to the radial case. The relaxation of the southern part of the magnetosphere showed denser plasma population up to $30R_E$ tailward and flared in toward north at around $25R_E$. The cavity around the planet position is smaller and more confined in the quasi-radial IMF than the radial IMF case.

Besides that, the 2D plasma distribution in the equatorial plane for radial IMF (Fig. 4C), shows the impact of the dipole tilt on the plasma distribution in both dusk and dawn directions. It is found that the magnetosheath contracts under the pressure of large populations in the bow shock which is larger on the dusk side than on the dawn side. Furthermore, particle entry inside the magnetosphere is largely distributed around the planet making the cavity reaches $\pm 5R_E$ on South-North direction and around $3R_E$ tailward, with plasma tube along the Sun-Earth line up the the planet position. While on the other hand, the effect of B_y for the quasi-radial IMF in Fig. 4D, shows the compressed magnetopause on both locations along OX and tilted magnetic equator axes. The cavity around the planet is more confined and reduced in size to $\pm 3R_E$ along south north and $\approx 1.4R_E$. The magnetospheric structure in the Dusk-Dawn plane for radial IMF (Fig. 4E) shows denser plasma in the dawn sector from 10 to $20 R_E$ than on the dusk side from -10 to $-20 R_E$, while in the northern sector of the magnetosphere there is a denser plasma that extends from around 10 to $17R_E$ but not regularly structured with same thickness in the southern sector. It appears that there is a finger like structure (particle entry) at around $5R_E$ on the dusk side that extends to around $1R_E$ in the cavity around the planet, on the other hand, for quasi-radial IMF the

plasma distribution contour shows smaller cavity size and denser plasma on the dusk side, with a large plasma structure starting at $10 - 20R_E$ dawn and $10R_E$ north and extends to $20R_E$ downward (Fig. 4F).

We use the data generated by IAPIC to plot the magnetic field topology that corresponds to the plasma distribution contours shown in Fig.4 to shed light on the differences and similarities between two IMF orientations along three different planes. In Fig. 5A the radial IMF field lines along OX are horizontal at $-20R_E$ and $\pm 3R_E$ along South-North direction and seen curled at $\pm 10R_E$. At the magnetopause position, the field lines divert at $f(x,z)=(-10, -8)R_E$. At dayside magnetosphere, there are two potential MR sites found at $f(x,z)=(0.5, -12) \& (-7.6, 11.9)R_E$. The magnetic field line topology shown in Fig. 5B is horizontal in the undisturbed SW, this was not the case in Fig. 5A. This difference is attributed to the impact of B_y . Potential MR sites are seen also at $f(x,z)=(-10.6, 9.1) \& (0.5, 10.1)R_E$. Constant attention should be made when looking at Fig.5C, taken in the equatorial plane, because of the dipole tilt what is shown here for radial IMF is the the high latitude magnetopause along OX in Dusk-Dawn direction. It is found that field lines from IMF connect to dipole field and permit particle entries at that latitudes. The wavy structure in the nightside (not the focus of the current study) indicates a complex current system induced at that distance. A potential MR site is shown at $f(x,y)=(-7.6, 9.9)R_E$. The curling of magnetic field lines at $f(x,y)=(5,-15), (-15,-7)R_E$ corresponds to the plasma dynamics shown in Fig. 4B. Same in Fig. 4D for quasi-radial IMF, the curled magnetic field lines at a latitude corresponding to $\approx 6R_E$ (north) are directed toward dusk-midnight direction. Potential MR sites are at $f(x,y)=(4.4,5.9), (-8.6,0.1), (3.5,-7.9)R_E$. In Fig. 4E, the dawn side magnetic field topology shows more extended structure of closed magnetic field lines until $\approx 14R_E$ toward dawn and reach up to $12R_E$ northward. In contrary, the quasi-radial IMF case in Dusk-Dawn plane shows different structure, where the extension of field lines is more important on the dusk side, but there are huge connections of planetary and interplanetary magnetic field lines and clear MR position at $f(y,z)=(-9.6,9),(3.4,-11.4)R_E$.

4.2 Dawn-Dusk asymmetry in the dayside magnetosphere under the influence of radial and quasi-radial IMF

. We report original results using our fully kinetic global code, IAPIC, to show the asymmetry in Dusk-Dawn and South-North directions for two IMF orientations one of which includes B_y as dominant. Quick visual overview for asymmetry is shown in Figures, 4, 6, 3, 14. Fig. 4C, D show the asymmetry in the Sun-Earth direction (OX) and Fig. 4E, F show the asymmetry along the Dusk-Dawn direction (OY). Linear densities are shown in Fig. 6 and plasma boundary layers in the equatorial and South-North planes can be seen in Fig. 3. In Fig. 14, plasma parameters are plotted in three locations for each IMF orientations, two of which are at $\pm 6R_E$ on both sides of OX axis, and the third along the Sun-Earth line along the simulation box length. More details are given in the next section 5 while these differences in numbers are shown for both IMF orientations in Tables 8 and 9. Asymmetry, a key result of this study, is shown for both IMF orientations on the dayside magnetosphere which tracks solar wind plasma on planes parallel to XZ until the measured magnetopause position. Therefore, values in both Tables 8 and 9 are quantifying the asymmetry in the magnetosheath in addition to the visual information reported in Fig. 14. In Table 8, solar wind parameters are measured for radial IMF along OX until the derived position of the magnetopause (MP= 10.4) but 6 R_E side way from OX on both dawn and dusk directions. Apparently there is a Dawn-Dusk asymmetry shown in Fig. 14 and in Table 8. In the same manner, the solar wind parameters are measured for quasi-radial IMF along OX until the magnetopause position ($10.98R_E$) at $6R_E$ on both directions toward dusk and dawn. Table 9 and Fig. 14B show the asymmetry for N_i , T_i , T_e , V_i , B_x , B_y and B_z .

itions were scaled for IAPIC as described in section 2. For purposes of comparison, we discuss in detail the plasma properties at the time step $3700\Delta t$ of our simulation for both full and quasi-radial IMF. This time step corresponds to ≈ 24 minutes of real time (based on scaled data relative to spatial and temporal resolution of the code), a relatively long enough period to perform kinetic simulation of the problem in hand. In the following, IAPIC

Parameter	Dawn ($Y = +6R_E$)	Dusk ($Y = -6R_E$)	OX ($Y=0$)	Dawn/dusk
N_i	8.626	19.151	5.446	0.450
T_i	0.005	0.003	0.006	1.4929
T_e	0.181	0.203	0.195	0.8930
V_i	0.063	0.033	-0.006	1.894
B_x	0.696	0.007	0.277	99.561
B_y	0.251	0.107	0.089	2.341
B_z	0.445	0.107	0.639	4.146

Table 5. Aiming to monitor the Dusk-Dawn asymmetry, plasma parameters are calculated at the derived magnetopause ($10.4 R_E$, see Table 7) for radial IMF for three vertical planes at $Y=-6,0,+6 R_E$ and averaged over $Z=4\Delta = 0.2R_E$.

Parameter	Dawn ($Y = +6R_E$)	Dusk ($Y = -6R_E$)	OX ($Y=0$)	Dawn/dusk
N_i	6.439	9.297	4.867	0.693
T_i	0.003	0.003	0.005	1.262
T_e	0.174	0.172	0.187	1.013
V_i	-0.009	0.073	0.025	-0.123
B_x	0.156	0.423	0.354	0.368
B_y	-0.385	-0.325	-0.186	1.184
B_z	0.100	-0.325	0.530	-0.307

Table 6. Aiming to monitor the Dusk-Dawn asymmetry, plasma parameters are calculated at the derived magnetopause ($10.98 R_E$, see Table 7) for quasi-radial IMF for three vertical planes at $Y = -6, 0, +6R_E$ and averaged over $Z=4\Delta = 0.2R_E$.

simulation results are analyzed to determine the magnetopause shape, size and location for the two IMF conditions assumed, which give us a good frame to characterize any dawn-dusk asymmetry in the system.

4.3 Magnetopause response to the full and quasi-radial IMF

We derive the magnetopause size using the steepening of the maximum radial density gradient (e.g., Garcia & Hughes, 2007; J. Lu et al., 2015). Because of the magnetic field axis tilt (31°), the system is inherently asymmetric and the Cartesian grid used in the IAPIC simulations is not adequate to accurately derive a density gradient in most planes, particularly in the magnetic equatorial plane. To overcome this difficulty, we transform our Cartesian 3D simulation box quantities (density, velocity vector, etc. at (x,y,z) positions) into a spherical 3D domain (same quantities at (r, θ, ϕ) positions), at the price of losing data from regions outside a spherical volume of radius equal to the smallest dimension of the initial Cartesian box (OY or OZ in our case). Our study does not suffer of that limitation because

the dayside MP, our region of interest, is located inside the selected spherical domain. After checking that both reference frames provide the same spatial distribution of all physical quantities along OX, OY, and OZ axis, we focus on deriving the magnetopause size at two key planes, namely the magnetic equatorial plane $\theta = -31^\circ$ and the plane $\theta = 0^\circ$ that contains the Sun-Earth line.

In a first step, we focus on the direction defined by $\phi = -180^\circ$ in both planes. We derive comparable values for the magnetopause position at $\sim 10.4, \sim 11.0$) R_E respectively for radial and quasi-radial IMF along Sun-Earth axis and equal to $(\sim 10.4, \sim 10.7)$ R_E when the effect of backstreaming ions is removed. However, along the tilted axis contained in the magnetic equatorial plane, the magnetopause positions are $(10.5, 11.8)$ R_E with bulk flow and equal to $10.8, 11.8 R_E$ without backstreaming ions, respectively for the two IMF conditions.

First, we note that the different magnetopause positions derived from the IAPIC simulation are all larger than the expected magnetopause position ($\sim 9.6 R_E$) derived from the classical $1/6$ power law corresponding to the initial solar wind parameters used in our simulations. All values derived show an expansion of the magnetopause position along the two selected axes but also sunward, as if the magnetopause is subject to a reduced SW pressure that allows the dipole magnetic field network to expand outward. It is remarkable that our model predicts the magnetopause expansion in the range $(1.4-2.2)$ R_E along Sun-Earth axis and Magnetic equator axis for quasi-radial IMF. This expansion range is consistent with MHD simulations and THEMIS observations shown by A. Samsonov et al. (2017) which reported magnetopause expansion in the range $(1.3-1.5)$ R_E . On the other hand and for purely radial IMF along the two axes, the magnetopause expands in the range $(0.8-0.9)$ R_E and therefore smaller than in the quasi-radial case.

In the following, we explore our (3D, 3V) IAPIC simulation results to try uncover potential processes that could be at the origin of the measured expansion. Since early reports on the expansion of the MP, several studies pointed to the potential impact of kinetic ef-

fects, particularly with the detection of the signature of particles streaming in a direction opposite to the solar wind (Spreiter & Alksne, 1969; Willis, 1978, 1978; Sibeck et al., 2001; A. Samsonov et al., 2017). As IAPIC simulations offer the access to all populations of particles (macro-particles) with specific kinetic properties, we tried to extract those particles on the dayside that move sunward, against the main impinging solar flow. That statistical sub-population of particles has its own kinetic properties and most importantly counter-balances the ram pressure of the incident solar flow, as if it was originating from the magnetosphere and flowing outward. It is important to stress that this population has kinetic properties (temperature, speed, etc) much different from the planetary ionospheric population that flows from the plasmasphere or the polar wind. In Fig. 2, bulk pressures (dynamic, thermal denoted P_{dyn} and P_{thm} respectively) are co-plotted with and without backstreaming ions to visualize the difference they make in the pressure balance. P_{dyn} and P_{thm} encounter P_{mag} at two points, i.e. with and without backstreaming ions included. Kinetically, the magnetopause is derived with the pressure balance that includes bulk contents which revealed the size of the MP, as $10.5R_E$ for radial IMF and $11.2R_E$ for quasi-radial IMF along the Sun-Earth axis. In the magnetosheath the thermal pressure is dominant over dynamic pressure. Importantly, if the backstreaming ion effect is dropped, then there should be contraction of the magnetopause size, which reads the values of 9.7 and $10.8R_E$ for same IMF orientations respectively. The magnetopause is also measured along the tilted magnetic equator axis with and without backstreaming ions and found equal to $11.2, 10.8R_E$ for radial IMF and $11.7, 11.1R_E$ for quasi-radial IMF, respectively. To summarize, these findings are tabulated in Table 7.

We report new results to track the magnetopause shape for both IMF orientations at two different locations namely along the Sun-Earth axis and along the tilted magnetic equator axis.

The equatorial plane is used to track the magnetopause shape using spherical coordinates ($\phi = -180^\circ$ at the dayside standoff distance) and ($\theta = 0$) along OX and ($\theta = -31$) along the magnetic equator axis of the tilted Earth's dipole field. We track the magnetopause shape

Maximum Density Steepening magnetopause derivation				
IMF /Axis	Sun-Earth Axis		Tilted Magnetic equator axis	
Kinetic effects	Yes	No	Yes	No
magnetopause for radial IMF	10.4 R_E	10.4 R_E	10.5 R_E	10.8 R_E
magnetopause for quasi radial	11.0 R_E	10.7 R_E	11.8 R_E	11.8 R_E
Pressure balance magnetopause derivation				
IMF/Axis	Sun-Earth Axis		Tilted Magnetic equator axis	
Kinetic effects	Yes	No	Yes	No
magnetopause for radial IMF	10.5 R_E	9.7 R_E	11.2 R_E	10.8 R_E
magnetopause for quasi radial	11.2 R_E	10.8 R_E	11.7 R_E	11.1 R_E

Table 7. Summary of results: magnetopause is derived in two different methods. One relies on density gradient maximum steeping and the other for pressure balance downstream of the bow shock. Both methods are derived along Sun-Earth Axis and along Tilted Magnetic equator axes. Additionally, magnetopause is derived when backstreaming ions are included (kinetic effect) and without them. The slight difference of the measurements in both methods emphasize the impact of density alone and the velocity and thermal pressure on the other hand on the magnetopause derivation (e.g., A. Samsonov et al., 2020). As per IAPIC result, magnetopause reads $[10.4, 11.0] R_E$ and $[10.5, 11.2] R_E$ for radial and quasi-radial IMF when measured by the density and pressure methods respectively

every 20° along ϕ in two different manners (e.g., Fig. 3), using maximum density gradient as reported in Table 7. For instance, for the two IMF orientations, we first compare magnetopause shapes in Fig. 3A, B respectively along Sun-Earth and the tilted magnetic equator axes. In a second step, we compare magnetopause shapes for the same IMF orientation as in Fig. 3C and D. The only difference between the two IMF orientations is the large B_y domination in quasi-radial case (case study compared with A. Samsonov et al. (2017)). The impact of B_y is clearly depicted and results in squeezing the magnetopause shape at around $8R_E$ on the dawn side and at around $12R_E$ on the dusk side on Sun-Earth line (Fig. 3A). Furthermore, the magnetopause shape for radial IMF is more flared out and extended in the equatorial plane up to $15R_E$, but both shapes expanded along Sun-Earth line up to 10.4 and 10.98 R_E , respectively. In Fig. 3B, the magnetopause shape is derived for both IMF orientations along the tilted magnetic axis. For radial IMF, it is more symmetric and more flared out than for quasi-radial IMF and the impact of B_y results in confining the global shape of the magnetopause along this direction. It is worth noting that in Fig. 3B, the part of the magnetopause in the dawn direction is more flattened because the plasma

flow dynamic pressure in this direction is larger than in the dusk direction (see Fig. 4C, D and Fig. 6.)

In Fig. 3C, the magnetopause shape is compared for the same IMF direction but at two different locations i.e. along the Sun-Earth and the tilted magnetic equator axes. The difference between the two shapes appears in the dawn-side portion of the MP. For the quasi-radial IMF, the confinement of the magnetopause due to the B_y effect is stronger along the Sun-Earth direction than along the tilted magnetic equator axis. In order to check the magnetopause location from the linear density profile in 3D, we use IAPIC data to plot the solar wind plasma density for both ions and electrons (Fig. 6A, B) for the two IMF directions in three planes from -20 to -10 R_E on OX, and -20 to 20 R_E on OY, and OZ. For the radial IMF, it is found that the inflow solar wind starts encountering the dipole field at the bow shock ($\approx 14R_E$). It is worth noting that the density should decrease to almost zero at the magnetopause position theoretically, but in our case there are still some plasma populations inside the magnetosphere along the Sun-Earth line, which is in agreement with experimental data (A. A. Samsonov & Pudovkin, 2000), additionally, it is practically difficult to account for perfect normal angle between incident solar wind and the magnetopause standoff boundary. Whilst, in Dusk-Dawn direction, the plasma boundary layer at $\pm 10R_E$ is asymmetric and is denser on the dusk side due to the effect of B_y . Furthermore, the structure in the South-North plane shows the two boundaries in asymmetric manner with the northern part having higher plasma density populations than the southern part.

On the other hand, for quasi-radial IMF, the linear density along OX has a double hump, tracking plasma inflow and the backstreaming ions/electrons, the plasma humagnetopause is seen at around $-16R_E$, and is apparently not due to backstreaming particles, and may be generated by wave-particle interactions (see Fig. 10, Fig. 8, and Fig. 9), this density humagnetopause did not appear in the radial IMF structure. The linear density along Dusk-Dawn shows the asymmetric boundary layer structure with higher density on the dawn side than on the dusk side while in the South-North direction the linear density shows a high peak of plasma of 1.5 times higher in the south region than in the northern

one.

The other major components of the solar wind dynamics is its velocity modulus that is shown in Fig. 7 in the same order. To better visualize a large scale image of the system, contour plotting is conducted to show the plasma density distribution and magnetic field topology in 3D as in Fig. 4 & 5. It is found that the planet tilt (31°) has a major impact on the global macro-structure of the magnetosphere in the simulation box of size ($\approx 60 \times 40 \times 40 R_E$). In Fig. 4A, when the forefront of the solar wind coplanar inflow approaches the magnetosheath it hits the upper boundary of the magnetopause before the tilted magnetic equator axis, this makes plasma override the boundary there before it reaches the lower boundary. This results in squeezing the magnetopause at high latitude and relaxes it in lower latitude thus making it flares out at around $20R_E$ (see also Fig. 3). There is around $6R_E$ vertical distance between the Sun-Earth and the tilted magnetic equator axes. Ionosphere is not included in the current study, as particles entry inside the magnetosphere is seen up to $5R_E$. The plasmasphere is shown up to $7R_E$. In Fig. 4B showing the plasma distribution for quasi-radial IMF, there is a plasma humagnetopause (hump) of $\approx 2.3R_E$ thickness between -17 and -14.5 along the Sun-Earth line and extended curve-linearly from -12 (south) to 7 (north) in a dome-like shape. It is not clear what causes this humagnetopause that is absent in the radial IMF case at the same time step. The dynamic pressure at both cusps is relatively equivalent contrary to the radial case. The relaxation of the southern part of the magnetosphere showed denser plasma population up to $30R_E$ tailward and flared in toward north at around $25R_E$. The cavity around the planet position is smaller and more confined in the quasi-radial IMF than the radial IMF case.

Besides that, the 2D plasma distribution in the equatorial plane for radial IMF (Fig. 4C), shows the impact of the dipole tilt on the plasma distribution in both dusk and dawn directions. It is found that the magnetosheath contracts under the pressure of large populations in the bow shock which is larger on the dusk side than on the dawn side. Furthermore, particle entry inside the magnetosphere is largely distributed around the planet making the cavity reaches $\pm 5R_E$ on South-North direction and around $3R_E$ tailward, with plasma tube

along the Sun-Earth line up the the planet position. While on the other hand, the effect of B_y for the quasi-radial IMF in Fig. 4D, shows the compressed magnetopause on both locations along OX and tilted magnetic equator axes. The cavity around the planet is more confined and reduced in size to $\pm 3R_E$ along south north and $\approx 1.4R_E$. The magnetospheric structure in the Dusk-Dawn plane for radial IMF (Fig. 4E) shows denser plasma in the dawn sector from 10 to 20 R_E than on the dusk side from -10 to -20 R_E , while in the northern sector of the magnetosphere there is a denser plasma that extends from around 10 to 17 R_E but not regularly structured with same thickness in the southern sector. It appears that there is a finger like structure (particle entry) at around 5 R_E on the dusk side that extends to around 1 R_E in the cavity around the planet, on the other hand, for quasi-radial IMF the plasma distribution contour shows smaller cavity size and denser plasma on the dusk side, with a large plasma structure starting at 10 – 20 R_E dawn and 10 R_E north and extends to 20 R_E downward (Fig. 4F).

We use the data generated by IAPIC to plot the magnetic field topology that corresponds to the plasma distribution contours shown in Fig.4 to shed light on the differences and similarities between two IMF orientations along three different planes. In Fig. 5A the radial IMF field lines along OX are horizontal at $-20R_E$ and $\pm 3R_E$ along South-North direction and seen curled at $\pm 10R_E$. At the magnetopause position, the field lines divert at $f(x,z)=(-10, -8)R_E$. At dayside magnetosphere, there are two potential MR sites found at $f(x,z)=(0.5, -12)\&(-7.6, 11.9)R_E$. The magnetic field line topology shown in Fig. 5B is horizontal in the undisturbed SW, this was not the case in Fig. 5A. This difference is attributed to the impact of B_y . Potential MR sites are seen also at $f(x,z)=(-10.6, 9.1)\&(0.5, 10.1)R_E$. Constant attention should be made when looking at Fig.5C, taken in the equatorial plane, because of the dipole tilt what is shown here for radial IMF is the the high latitude magnetopause along OX in Dusk-Dawn direction. It is found that field lines from IMF connect to dipole field and permit particle entries at that latitudes. The wavy structure in the nightside (not the focus of the current study) indicates a complex current system induced at

that distance. A potential MR site is shown at $f(x,y)=(-7.6, 9.9)R_E$. The curling of magnetic field lines at $f(x,y)=(5,-15), (-15,-7)R_E$ corresponds to the plasma dynamics shown in Fig. 4B. Same in Fig. 4D for quasi-radial IMF, the curled magnetic field lines at a latitude corresponding to $\approx 6R_E$ (north) are directed toward dusk-midnight direction. Potential MR sites are at $f(x,y)=(4.4,5.9), (-8.6,0.1), (3.5,-7.9)R_E$. In Fig. 4E, the dawn side magnetic field topology shows more extended structure of closed magnetic field lines until $\approx 14R_E$ toward dawn and reach up to $12R_E$ northward. In contrary, the quasi-radial IMF case in Dusk-Dawn plane shows different structure, where the extension of field lines is more important on the dusk side, but there are huge connections of planetary and interplanetary magnetic field lines and clear MR position at $f(y,z)=(-9.6,9),(3.4,-11.4)R_E$.

4.4 Dawn-Dusk asymmetry in the dayside magnetosphere under the influence of radial and quasi-radial IMF

. We report original results using our fully kinetic global code, IAPIC, to show the asymmetry in Dusk-Dawn and South-North directions for two IMF orientations one of which includes B_y as dominant. Quick visual overview for asymmetry is shown in Figures, 4, 6, 3, 14. Fig. 4C, D show the asymmetry in the Sun-Earth direction (OX) and Fig. 4E, F show the asymmetry along the Dusk-Dawn direction (OY). Linear densities are shown in Fig. 6 and plasma boundary layers in the equatorial and South-North planes can be seen in Fig. 3. In Fig. 14, plasma parameters are plotted in three locations for each IMF orientations, two of which are at $\pm 6R_E$ on both sides of OX axis, and the third along the Sun-Earth line along the simulation box length. More details are given in the next section 5 while these differences in numbers are shown for both IMF orientations in Tables 8 and 9. Asymmetry, a key result of this study, is shown for both IMF orientations on the dayside magnetosphere which tracks solar wind plasma on planes parallel to XZ until the measured magnetopause position. Therefore, values in both Tables 8 and 9 are quantifying the asymmetry in the magnetosheath in addition to the visual information reported in Fig. 14. In Table 8, solar wind parameters are measured for radial IMF along OX until the derived position of the

magnetopause (MP= 10.4) but $6 R_E$ side way from OX on both dawn and dusk directions.

Apparently there is a Dawn-Dusk asymmetry shown in Fig. 14 and in Table 8. In the

same manner, the solar wind parameters are measured for quasi-radial IMF along OX until

the magnetopause position ($10.98 R_E$) at $6 R_E$ on both directions toward dusk and dawn.

Table 9 and Fig. 14B show the asymmetry for N_i , T_i , T_e , V_i , B_x, B_y and B_z .

Parameter	Dawn ($Y = +6R_E$)	Dusk ($Y = -6R_E$)	OX ($Y=0$)	Dawn/dusk
N_i	8.626	19.151	5.446	0.450
T_i	0.005	0.003	0.006	1.4929
T_e	0.181	0.203	0.195	0.8930
V_i	0.063	0.033	-0.006	1.894
B_x	0.696	0.007	0.277	99.561
B_y	0.251	0.107	0.089	2.341
B_z	0.445	0.107	0.639	4.146

Table 8. Aiming to monitor the Dusk-Dawn asymmetry, plasma parameters are calculated at the derived magnetopause ($10.4 R_E$, see Table 7) for radial IMF for three vertical planes at $Y=-6,0,+6 R_E$ and averaged over $Z=4\Delta = 0.2R_E$.

Parameter	Dawn ($Y = +6R_E$)	Dusk ($Y = -6R_E$)	OX ($Y=0$)	Dawn/dusk
N_i	6.439	9.297	4.867	0.693
T_i	0.003	0.003	0.005	1.262
T_e	0.174	0.172	0.187	1.013
V_i	-0.009	0.073	0.025	-0.123
B_x	0.156	0.423	0.354	0.368
B_y	-0.385	-0.325	-0.186	1.184
B_z	0.100	-0.325	0.530	-0.307

Table 9. Aiming to monitor the Dusk-Dawn asymmetry, plasma parameters are calculated at the derived magnetopause ($10.98 R_E$, see Table 7) for quasi-radial IMF for three vertical planes at $Y = -6, 0, +6R_E$ and averaged over $Z=4\Delta = 0.2R_E$.

5 Discussion and Analysis

The goal set for our paper is to use a kinetic code to study the impact of radial and quasi-radial IMF and solar wind pressure balance systems on the dynamics of the magnetosphere, and their impact on magnetopause size, location and shape, in addition to the asymmetry that resulted from the interaction. For reference, many studies tend to support that when the IMF is close to radial orientation, it has strong impact on the magnetopause location due in part to the reduction of the pressure and variation of the IMF that originates in an expanded foreshock (e.g., Blanco-Cano et al., 2009b; Gutynska et al., 2015) resulting in magnetopause expansion (Sibeck et al., 2000; Shue et al., 2009; Korotova et al., 2011), and in part to effects connected with a transformation of the radial magnetic field orientation in the magnetosheath (Pi et al., 2018). However, few modeling efforts have explicitly studied kinetic effects, particularly for the indicated IMF cases. In the following, we discuss the findings of the IAPIC modeling of the magnetospheric event adopted from MHD simulation and THEMIS observation reported in (A. V. Suvorova et al., 2010; A. Samsonov et al., 2017).

As described in section 4.3, we derived the magnetopause size under the specified solar wind conditions and IMF orientation by two different methods, namely the maximum steepening of plasma density and the balance between ram pressure and magnetic pressure. First, we used the maximum plasma density function derived with respect to radial distance along $\phi = 180^\circ$ on dayside at two locations corresponding to $\theta = 0^\circ$ along Sun-Earth line and $\theta = 31^\circ$ along tilted magnetic equator axis. This method shows the magnetopause position at (10.4,11.0) R_E for purely and quasi-radial IMF, respectively. As described in the previous section, PIC simulations offer the possibility to isolate backstreaming ions from the pool of particles in the box simulation, which allows us to derive their contribution to the dynamic and thermal pressures in the dayside magnetosphere. It is important to stress that other complex effect could be induced by the presence of those backstreaming particles, like induced currents and fields, that will be considered in a future study. The fact to cancel

the participation of backstreaming ions in the ensemble average of the plasma properties, increases the system pressure and consequently moves the magnetopause location toward Earth. The pressure balance method used in our paper to derive the magnetopause position is based on kinetic approach to describe the counter balance of dynamic and thermal pressure in the solar wind and the magnetosheath with the dipole field. This approach is microscopic in general term taking into account the backstreaming ions effect, which is essentially the same as the macroscopic approach (continuum fluid treatment). This treatment of microscopic and macroscopic approaches were discussed in the past (Heikkila, 1975; Willis, 1978; Spreiter & Stahara, 1984).

Using the balance between ram pressure and magnetic pressure, (e.g., Willis, 1978, Eq. 3) without accounting for backstreaming ions the magnetopause is measured equal to $(9.7, 10.8)R_E$ for radial and quasi-radial IMF respectively, whereas when backstreaming ions are included, we get $(10.5, 11.2)R_E$ along the Sun-Earth line (see Fig. 2). The magnetopause is measured along the tilted magnetic equator axis ($\theta = 31^\circ$) and found equal to 10.8, $11.1R_E$ and to 11.2, $11.7R_E$ without and with backstreaming ions in the flow for radial and quasi-radial IMF respectively.

We conclude that the dynamic pressure of backstreaming ions potentially contribute to the expansion/compression of the magnetopause even if that contribution is small, therefore they should not be ignored and should be accounted for. For example, when magnetopause is derived from density maximum steepening, the backstreaming ion effect was very small and in one case was absent. But, when the magnetopause is derived from pressure system balance, the absence of backstreaming ions from calculations results to a compression of the magnetopause by $(0.8, 0.6R_E)$ for radial IMF along the two axis and a compression of $(0.4, 0.6R_E)$ for quasi-radial IMF along the two axis. That is to say, the main driver of the expansion of the magnetopause is the reduction of the solar wind dynamic pressure and along with the IMF orientation, namely radial/quasi-radial IMF in this case. This result leads us to the conclusions reported in (A. Samsonov et al., 2020, Eq. 2), that density

and velocity (dynamic pressure) might have different contributions to the effective values of the dynamic pressure component in the pressure system balance used in driving the magnetopause position. This appears clearly in our results in Table 7 in the upper two rows.

In their MHD model using a global reduction of the solar wind dynamic pressure, A. Samsonov et al. (2017) found that the magnetopause expands on average between $1.3 - 1.5R_E$ which was consistent with expansion observed by THEMIS spacecraft and in agreement with $\approx 1.4R_E$ average expansion reported in the statistical study by (Dušík et al., 2010). In our study, we found a self-consistent magnetopause expansion of $1.6R_E$ for quasi-radial IMF, which is consistent with A. Samsonov et al. (2017), while the expansion rate is $0.9R_E$ for purely radial IMF along Sun-Earth axis. The expansion rate for the two IMF orientations along ($\theta = 31^\circ$) is $1.6-2.1R_E$. This agreement between MHD and IAPIC is important to use the models in a complementary manner and to better understand the physics of atypical events in space plasma physics.

In order to visualize the macrostructure of the plasma distributions and magnetic field topology in our 3D simulation box, three figures are added to this study. For example, in Fig. 4 the plasma distribution for the macrostructure of the Earth's magnetosphere is shown. The dipole tilt is clearly depicted in Fig. 4A, B. The equatorial plane of Fig. 4C, D are along Sun-Earth axis only. The linear plot of this figure is shown in Fig. 6.

The corresponding magnetic field streamlines are shown in Fig. 5. The wavy structure of the magnetic field lines topology shown in 3D led us to discuss the correlation coefficients (CC) of the magnetic field components along the Sun-Earth axis (averaged over $\approx 1R_E$ along the dawn-dusk direction) between the undisturbed solar wind and the magnetosheath. These CC calculation aims at studying if the change of the magnetic field is local or global. It is found that the CC for $B_z \approx 0.74$ is higher than for $B_y \approx 0.32$, but it is poor and negative for $B_x \approx -0.1$ for radial IMF which is likely the consequence of the draping of the magnetic field lines around the magnetosphere. On the other hand, the CC for quasi-radial

IMF is found close in value for B_x & $B_z \approx (0.26, 0.3)$, whilst it is ≈ 0.13 for B_y . These small CC values suggest that the presence of the B_y component leads to strong magnetic field changes in the magnetosheath. Similar discussion is reported in (e.g., Pi et al., 2016), where authors used data from OMNI and THEMIS to compare magnetic structure in the SW and the magnetosheath. The authors found that the CC is better for B_z than B_y and is poor for B_x . Finally, we computed CC between ion and electron densities shown in Fig. 6C,D, and found values ≈ 1 , indicating that no charge separation occurs along the simulation box.

To better understand the kinetics of the distribution of the backstreaming ions, we present two figures 8 and 9. In Fig. 8 a full range of the simulation box size shows the global ion velocity spatial distribution for both IMF orientations. Fig. 8A,B show the concentration of the backstreaming ions close to the bow shock and magnetosheath, with some minor plasma population inside the magnetosphere. Fig. 8C,D confirms the distribution in A&B when plotted in Dusk-Dawn direction and E&F when plotted in South-North axis as well. This figure globally reveals an overall image of the velocity inflow/outflow and shows relative percentage of the backstreaming ions along the 3D simulation box. The velocity distribution function (VDF) of solar wind ions as far as $-20R_E$ along Sun-Earth line is shown in Fig. 9. For the purely radial IMF case ($B = B_x$), a substantial fraction of backstreaming ions is found in the three planes (XZ, XY and YZ) whereas only a small fraction is obtained for quasi-radial IMF especially in the YZ plane. The contribution of B_y impacts the particle distribution flow is depicted in XZ-plane.

Some of the other featured results of this kinetic study such as the link between pressure systems in different regions in the dayside magnetosphere and the ion/electron temperature anisotropy are discussed here. For example, in Table 10 we show the dynamic, thermal and magnetic pressures values (fractions) in the magnetosheath at $\pm 3 R_E$ at the subsolar point for both IMF directions.

We found the $P_{thm}/P_{dyn} \approx 13$ at $3R_E$ inside the magnetosphere for radial IMF along Sun-Earth line. The same ratio reads and ≈ 1.6 for quasi-radial IMF on the same axis. This table not only answers the question of what fraction does the solar wind dynamic pressure

Table 10. This table shows the pressure system values along OX at $\pm 3 R_E$ from the measured MP position for both IMF orientations. The table values suggest that backstreaming ions should be accounted for in pressure balance between SW dynamic pressure and thermal pressure, and the dipole magnetic pressure (see Fig. 2). In the magnetosheath the ratio P_{thm}/P_{dyn} is $\approx (12.75, 1.64)$ for radial and quasi-radial IMF, respectively.

IMF	dynamic		thermal		magnetic	
MP \pm	$+3R_E$	$-3R_E$	$+3R_E$	$-3R_E$	$+3R_E$	$-3R_E$
radial	0.004	0.003	0.051	0.004	0.03	0.31
MP \pm	$+3R_E$	$-3R_E$	$+3R_E$	$-3R_E$	$+3R_E$	$-3R_E$
quasi	0.017	0.001	0.028	0.005	0.058	0.22

applies on the magnetosphere (e. g., A. V. Suvorova et al., 2010) but shows the potential backstreaming particle contribution to dynamic and thermal pressures (electron contribution is included) when encountering the dipole pressure at the magnetopause (see Table 7, Fig. 2 and Fig. 10) as well. Additionally, the average location of the magnetopause was derived based on these inputs for the two IMF directions. These effects are absent from global MHD and hybrid codes. We concluded from the pressure study, that when backstreaming ions are removed from the bulk flow, the incident dynamic and thermal pressure will increase and result in compressing the magnetopause earthward. It is worth noting that Fig. 10A,B plotted in spherical coordinates (radial distance from the Earth) along Sun-Earth axis for radial and quasi-radial IMF respectively and similarly Fig. 10C,D plotted along the tilted magnetic equator axis show the bulk flow (red) versus the backstreaming ions (blue) from almost the MP position up to $20R_E$ in the dayside magnetosphere. For radial IMF, the ratio of flow density to the back scattered ion density is ≈ 5 . Backstreaming ions velocity is measured at one point ($\approx 12R_E$) in the magnetosheath and found equal to 250 & 190 km.sec $^{-1}$ for radial IMF along Sun-Earth and tilted magnetic equator axes respectively. Similarly, for quasi-radial IMF, these values read 140 & 149 km.sec $^{-1}$. The flow and backstreaming ions are tabulated in Table 11 for comparison. These values are in agreement with (Shue et al., 2009).

As per temperature anisotropy in Fig. 11C it is found that $T_{i\perp}/T_{i\parallel} = 1.8$ for radial IMF, with correlations coefficient ($C.C.$) $\approx 0.23, -0.07$ for ions and electrons respectively. More-

Table 11. This Table shows the SW plasma velocity measured at one point $\approx 12R_E$ in the magnetosheath. At each axis SW velocities are compared in terms of inflow/outflow values. It shows that for radial IMF the sunward flow is faster in the magnetosheath.

IMF	Sun-Earth		Tilted magnetic equator	
	inflow (km.sec ⁻¹)	outflow (km.sec ⁻¹)	inflow (km.sec ⁻¹)	outflow (km.sec ⁻¹)
Radial	91.3	250	189.7	48.5
Quasi-radial	140	140	63.5	149

over, we found also a perpendicular temperature anisotropy for electron: $T_{e\perp}/T_{e\parallel} = 2.2$. These values read a strong *C.C.* of ≈ 0.8 for ions with $T_{i\perp}/T_{i\parallel} \approx 6$ and anti-correlations for electrons ≈ -0.53 for quasi-radial IMF with $T_{e\perp}/T_{e\parallel} = 1.6$. (Fig. 11D). In-situ observations by the WIND spacecraft have shown that the temperature anisotropy at 1 AU is limited for ions $0.1 \leq R_a \leq 10$ as well as for electrons $0.5 \leq R_a \leq 2$ (e. g., Vafn et al., 2019; Bale et al., 2009), where $R_a = T_{\perp}/T_{\parallel}$ is the temperature anisotropy defined by perpendicular to parallel temperature ratio. These results are consistent with our findings for the anisotropic temperature ratios. From recent MMS observations, Maruca et al. (2018) discussed the proton temperature anisotropy ratio ($R_i = T_{\perp i}/T_{\parallel i}$) in relation with the parallel component of the plasma beta $\beta_{\parallel} = \frac{n_i k_B T_{\parallel i}}{B^2/(2\mu_0)}$. They reported as β_{\parallel} increase within a narrow range of R_i (we report in Fig. 11 that β_{\parallel} increases in range of -14to-12 R_E), the authors also found that by using data from MMS mission to explore the β_{\parallel} -dependents limits on the anisotropic ratio R_i . We show this result in Fig. 12.

The second major finding of this study is the Dawn-Dusk asymmetry. Asymmetry can directly results in dawn dusk asymmetric space weather effects, so uncovering its physics origin is important for better understanding, modeling and prediction of the space weather phenomena (e. g., S. Lu et al., 2016). Asymmetry is observed by Cluster spacecraft in north-south magnetotail planes (Haaland et al., 2017; A. Samsonov, 2006) and in dawn-dusk planes (A. P. Walsh et al., 2014; A. A. Samsonov, 2011; Dimmock et al., 2017; Turc et al., 2020). Both observations and numerical simulations have revealed that the magnetopause

size is a function of IMF strength and orientation, and solar wind dynamic pressure, which by turn modify the magnetopause shape and generate dawn-dusk asymmetries (Liu et al., 2019). Using data from Imagnetopause 8 and ISEE,1, ISEE, 3 and WIND, Paularena et al. (2001) showed a significant dawn-dusk asymmetry in the Earth's magnetosheath which is larger on the dawn side than on the dusk side. They also showed that the IMF orientation impacts density asymmetry in dawn-dusk direction. Paularena et al. (2001) reported same kind of asymmetry in different regions in the dayside magnetosphere in Sun-Earth and Dusk-Dawn planes. In their recent study, Turc et al. (2020) discussed the magnetosheath asymmetry in terms of IMF, solar wind density, velocity by using Vlasiator hybrid code (Palmroth et al., 2018). They found that magnetic field asymmetry and density variability in the magnetosheath are stronger when IMF tends toward a radial direction. Similarly, using IAPIC, the dawn-dusk asymmetry in the magnetosheath and in the solar wind is investigated. It is found that the magnetic field in the magnetosheath is larger on the dawn side than on the dusk side, and it changes its polarity on dawn direction for radial IMF. It is also found that there is anti-correlation between the magnetic field in the magnetosheath and in the solar wind and the best correlation is found equal 0.74 for IMF z-component in the radial case. It is worth noting that there is no change of polarity of the magnetic field in the magnetosheath for quasi-radial IMF. The new result of the derivation of the magnetopause size shows apparent dusk-dawn asymmetry for both IMF orientations, for example, in Fig. 3, taken in the equatorial plane, the asymmetry is clearly depicted.

To better display the asymmetry in the dayside magnetosphere, a cut in the XZ plane is taken in the simulation box from -20 to -10 R_E and at planet position in $Y=Z=0$. We chose to plot parameters at $6R_E$ on both dawn and dusk directions (e.g., S. Lu et al., 2016, Fig. 2). The following physical parameters are plotted in 3-planes (parallel to XZ-plane) N_i , T_i , T_e , V_i , B_x , B_y , and B_z (see Fig. 14) for both IMF orientations. Fig. 14 shows the different values at $\pm 6R_E$ from the Sun-Earth line. For example, looking at N_i in three cuts for both IMF orientations depicts clearly that N_i shows different values along OX asymmetrically. These SW parameters are quantified and tabulated in Tables 8 and 9 taken at $\pm 6R_E$ along

OX lines for both IMF orientations.

Finally, our analysis of the location, shape and size of the MP with the techniques developed for that purpose, in addition to the ability to quantify plasma parameters in 3D to track asymmetries in the dusk-dawn and south-north direction our code is applicable to planetary and exoplanetary magnetospheres. Furthermore, our findings can also contribute to alternative methods for soft x-ray imaging the magnetosphere (Sibeck et al., 2018) in a complementary manner. This includes the MP, the cusp dynamics, the magnetosheath that is related to density structure which can be deduced from soft x-ray observation.

Most current support to the smile mission is based on MHD modeling (smile working group). In light of the results obtained so far (see Fig. 2 & 3 , and Tables 7 & 11), our global 3D electromagnetic kinetic code is providing another point of view on the range of expected boundary locations under various solar wind flux. An accurate estimation of those boundary locations are key to interpret X-ray signal that will be detected by SXI, the Smile X-ray detector. In addition, our simulations provide details about ions kinetic properties locally and on global scales (eg. Fig. 6-10), an additional tool for coupling plasma properties that will be detected by the light Ion Analyser (LIA) and large scale structure that will be imaged by SXI. In light of the results obtained so far, we propose IAPIC, as a global 3D electromagnetic kinetic code to simulate the MP, the cusps, and the magnetosheath, which should enhance the science return of space missions like the CSA – ESASMILE mission.

6 Summary and Conclusion

We have utilized a three-dimensional kinetic particle-in-cell code (IAPIC) to determine the location and shape of Earth's magnetopause for a dipole tilt of 31° in response to the solar wind regimes of radial ($\mathbf{B}=\mathbf{B}_x$) and quasi-radial ($\mathbf{B}_z < \mathbf{B}_x, \mathbf{B}_y$) IMF. The simulations predict a highly asymmetric magnetosphere in both cases. The findings of this study are summarized as follows:

1. The simulated magnetopause expands from 9.6 to $11.0R_E$ along the Sun-Earth axis and from 9.6 to $11.8R_E$ along the tilted magnetic equator axis for quasi-radial IMF. In this case the expansion of magnetopause at both axes is 1.6 and $2.2R_E$ quite consistent with THEMIS observations which reported an average expansion of 1.3 - $1.5R_E$ (Jelínek et al., 2010; A. V. Suvorova et al., 2010), without being forced to modify the input solar wind parameters as done by MHD model (A. Samsonov et al., 2017).
2. For a purely radial IMF ($\mathbf{B}=\mathbf{B}_x$), the simulated magnetopause size only expands from 9.6 to $10.4R_E$ along Sun-Earth axis and from 9.6 to $10.5R_E$ along the tilted magnetic equator axis corresponding to an expansion range of 0.9 - $1.6R_E$. This case differs from quasi-radial IMF case, mostly by the absence of domination of B_y IMF. Therefore, B_y enhances the magnetopause expansion. In addition, in the quasi-radial case, the sunward expansion is larger but the earthward compression along the dawn-dusk direction is stronger.
3. The results reported in Fig. 2 and Table 7 draw a conclusion that the backstreaming ions impact on magnetopause derivation by using density steepening method is small or zero like the case of radial IMF along OX axis. In contrast, when magnetopause is derived using pressure system balance, backstreaming ions compress the magnetopause by ranges $\approx 0.4 - 0.8 R_E$ for radial and $\approx 0.4 - 0.6 R_E$ along OX and tilted magnetic equator axes for radial and quasi-radial IMF respectively.

- 880 4. The difference between magnetopause derivation using maximum density steepening
881 (Garcia & Hughes, 2007; J. Lu et al., 2015) and the pressure systems balance using
882 definition of dynamic pressure as in (e.g., Willis, 1978, Eq. 3) is consistent with
883 the conclusion drawn by (A. Samsonov et al., 2020), where the authors showed that
884 density and velocity act differently as a component of dynamic pressure in the pressure
885 system balance.
- 886 5. We present new results to show the magnetopause shape in spherical polar coordi-
887 nates for the two IMF directions. This new technique along with the magnetopause
888 derivations in Table 7 and Fig. 2 enables us to anticipate the sizes, shapes and loca-
889 tions of magnetopause for all magnetized planets, including magnetized exoplanets.
890 Additionally, this technique accounts for the backstreaming ion contribution to the
891 data used to derive the magnetopause shape, a technique that is not doable with
892 other types of simulations.
- 893 6. The current study enabled us to derive the solar wind temperature anisotropy, thus
894 paving a research road to study kinetic microinstabilities in the solar wind-magnetosphere
895 coupling (see Fig. 11 and 12). For quasi-radial IMF, T_{\perp}/T_{\parallel} is large and equal ≈ 6 for
896 ions and ≈ 1.6 for electrons. On the other hand, the T_{\perp}/T_{\parallel} for radial IMF equal to
897 1.8 and 2.2 for ions and electrons respectively.
- 898 7. The 3D velocity distribution function (Fig. 9) shows that backstreaming ions ap-
899 pear upstream to distances of about $-20R_E$. Draping of the IMF, and temperature
900 anisotropy in the magnetosheath, give rise to a complex structure that results in the
901 observed asymmetry in the dawn-dusk and north-south directions. The dawn-dusk
902 asymmetry is resolved in the current paper in tracking solar wind parameters at
903 $\pm 6R_E$ planes parallel to OX plane. In Tables 8 and 9, and in Fig. 14, the asymmetry
904 is depicted for both IMF orientations.
- 905 8. In light of the obtained results so far, our findings are considered an additional and key
906 modeling supports to future near-Earth exploration projects, particularly the SMILE
907 mission, in additions to outer planets moons and magnetospheres.

7 Future directions

Radial and quasi-radial conditions are relatively infrequent configurations of the IMF at Earth, but closer to the Sun, the Parker spiral becomes more and more radial. This suggests that radial IMF conditions are more common at Mercury, which has recently been investigated by MESSENGER and will soon be visited by the BepiColombo spacecraft. Furthermore, Mercury’s magnetosphere is much smaller as the magnetopause standoff position is only at about $2R_M$ (R_M being the Mercury radius) and the ion gyroradius is about the size of the planet. Finite Larmor radius effects are expected to play an ever more important role than in the Earth’s case (e.g., Johnson et al., 2014; Paral & Rankin, 2013). Mercury is therefore a natural laboratory for investigating radial IMF and related kinetic effects and we will prepare simulations in advance of BepiColombo’s arrival at Mercury.

Planets even closer to their stars are common in the galaxy (NASA Exoplanets Archive *doi* = 10.26133/NEA2), suggesting that, particularly around cooler M- and K-type stars, radial IMF may be a common condition. This impacts the structure of their magnetospheres and may influence the escape of planetary atmospheric and ionospheric constituents over time. The kinetic aspect of our approach is particularly sensitive to the dynamics of the bow shock, which may be highly variable in the neighborhood of a small star (Cohen et al., 2015), potentially producing accelerated particles and observable radio emissions (Cohen et al., 2018).

One more issue that will be considered for near future work is the impact of the magnetosphere-ionosphere-magnetosheath coupling on magnetopause location. We have tracked in the past H^+ and O^+ ions outflow from the ionospheric origin in the dayside magnetosphere (S. M. Baraka & Ben-Jaffel, 2015). IAPIC can also be used to study outflow of plasmasphere low energy ions.

Acknowledgments

This work is carried out using binary data generated by IAPIC, a pic code that is modified version of the Tristan code that is available to public through github: <https://github.com/ntoles/tristan-mp-pitp>. The used data for generating results is available at (https://zenodo.org/record/4436755#.X_8axi2970o). S Baraka acknowledges the NIA NASA grant # NNX15AE05G for supporting this research via the Living and Breathing Planet project. L. Ben-Jaffel acknowledges support from CNES under project PACES. S. Baraka thanks IAP-CNRS for using their computing resources facilities. Also S Baraka thanks Daniel Pomarede from Atomic Energy Commission, CNRS, France for providing SDvision software.

References

- Akasofu, S.-I. (1991). Development of magnetospheric physics. *Magnetospheric Substorms*, 64, 3–9.
- Akasofu, S.-I., Roederer, M., & Krimigis, S. (1982). Dawn-dusk asymmetry of the tail region of the magnetosphere of saturn and the interplanetary magnetic field. *Planetary and Space Science*, 30(10), 1061–1063.
- Artemyev, A., & Zelenyi, L. (2012, December). Kinetic Structure of Current Sheets in the Earth Magnetotail. *Space Science Reviews*, 178(2-4), 419–440. doi: 10.1007/s11214-012-9954-5
- Asbridge, J., Bame, S., & Strong, I. (1968). Outward flow of protons from the earth’s bow shock. *Journal of Geophysical Research*, 73(17), 5777–5782.
- Bale, S., Kasper, J., Howes, G., Quataert, E., Salem, C., & Sundkvist, D. (2009). Magnetic fluctuation power near proton temperature anisotropy instability thresholds in the solar wind. *Physical review letters*, 103(21), 211101.
- Baraka, S. (2016, April). Large Scale Earth’s Bow Shock with Northern IMF as Simulated by PIC Code in Parallel with MHD Model. *Journal of Astrophysics and Astronomy*, 37(2), 1–16. doi: 10.1007/s12036-016-9389-6
- Baraka, S., & Ben-Jaffel, L. (2007, June). Sensitivity of the Earth’s magnetosphere to solar wind activity: Three-dimensional macroparticle model. *Journal of Geophysical Research (Space Physics)*, 112, 6212. doi: 10.1029/2006JA011946
- Baraka, S., & Ben-Jaffel, L. (2011). Impact of solar wind depression on the dayside magnetosphere under northward interplanetary magnetic field. *Annales Geophysicae*, 29(1), 31–46. Retrieved from <https://www.ann-geophys.net/29/31/2011/> doi: 10.5194/angeo-29-31-2011
- Baraka, S. M., & Ben-Jaffel, L. (2015). Magnetospheric dynamical and morphological response to multi-species plasma supply from the ionosphere: New comprehensive 3d pic simulation. *AGUFM*, 2015, SM23B–2552.
- Ben-Jaffel, L., & Ballester, G. (2013, May). Hubble Space Telescope detection of oxygen in the atmosphere of exoplanet HD 189733b. *Astronomy & Astrophysics*, 553, A52. doi: 10.1051/0004-6361/201221014
- Ben-Jaffel, L., & Ballester, G. E. (2014, April). Transit of Exomoon Plasma Tori: New Diagnosis. *apjl*, 785, L30. doi: 10.1088/2041-8205/785/2/L30
- Berchem, J., Richard, R. L., Escoubet, C. P., Wing, S., & Pitout, F. (2016, January). Asymmetrical response of dayside ion precipitation to a large rotation of the imf. *Journal of Geophysical Research (Space Physics)*, 121, 263–273. Retrieved from <https://ui.adsabs.harvard.edu/abs/2016JGRA..121..263B> doi: 10.1002/2015JA021969
- Blanco-Cano, X., Omid, N., & Russell, C. (2006). Macrostructure of collisionless bow shocks: 2. ULF waves in the foreshock and magnetosheath. *Journal of Geophysical Research: Space Physics (1978–2012)*, 111(A10).
- Blanco-Cano, X., Omid, N., & Russell, C. (2009a). Global hybrid simulations: Foreshock waves and cavitons under radial interplanetary magnetic field geometry. *Journal of Geophysical Research: Space Physics*, 114(A1).
- Blanco-Cano, X., Omid, N., & Russell, C. (2009b). Global hybrid simulations: Foreshock

- waves and cavitons under radial interplanetary magnetic field geometry. *Journal of Geophysical Research: Space Physics*, 114(A1).
- Bobra, M., Petrinen, S., Fuselier, S., Claffin, E., & Spence, H. E. (2004). On the solar wind control of cusp aurora during northward imf. *Geophysical research letters*, 31(4).
- Brackbill, J. U. (2011). A comparison of fluid and kinetic models of steady magnetic reconnection. *Physics of Plasmas (1994-present)*, 18(3), 032309. doi: 10.1063/1.3568828
- Buneman, O., Neubert, T., & Nishikawa, K.-I. (1992). Solar wind-magnetosphere interaction as simulated by a 3-d em particle code. *IEEE transactions on plasma science*, 20(6), 810–816.
- Cai, D., Esmaeili, A., Lembège, B., & Nishikawa, K.-I. (2015). Cusp dynamics under northward imf using three-dimensional global particle-in-cell simulations. *Journal of Geophysical Research: Space Physics*, 120(10), 8368–8386.
- Cai, D., Li, Y., Nishikawa, K.-I., Xiao, C., Yan, X., & Pu, Z. (2003). Parallel 3-D Electromagnetic Particle Code Using High Performance FORTRAN: Parallel TRISTAN. In *Space Plasma Simulation* (Vol. 615, pp. 25–53). Springer Berlin Heidelberg. doi: 10.1007/3-540-36530-3_2
- Cohen, O., Ma, Y., Drake, J. J., Gloer, A., Garraffo, C., Bell, J. M., & Gombosi, T. I. (2015, jun). THE INTERACTION OF VENUS-LIKE, m-DWARF PLANETS WITH THE STELLAR WIND OF THEIR HOST STAR. *The Astrophysical Journal*, 806(1), 41. Retrieved from <https://doi.org/10.1088/0004-637x/806/1/41> doi: 10.1088/0004-637x/806/1/41
- Cohen, O., Moschou, S.-P., Gloer, A., Sokolov, I. V., Mazeh, T., Drake, J. J., ... Alvarado-Gómez, J. D. (2018, oct). Exoplanet modulation of stellar coronal radio emission. *The Astronomical Journal*, 156(5), 202. Retrieved from <https://doi.org/10.3847/1538-3881/aae1f2> doi: 10.3847/1538-3881/aae1f2
- Dimmock, A., Nykyri, K., Osmane, A., Karimabadi, H., & Pulkkinen, T. (2017). Dawn-dusk asymmetries of the earth's dayside magnetosheath in the magnetosheath interplanetary medium reference frame. *Dawn-Dusk Asymmetries in Planetary Plasma Environments*, 49–72.
- Dušík, Š., Granko, G., Šafránková, J., Němeček, Z., & Jelínek, K. (2010). Imf cone angle control of the magnetopause location: Statistical study. *Geophysical Research Letters*, 37(19).
- Eastwood, J. P. (2008). The science of space weather. *Philosophical Transactions of the Royal Society A: Mathematical, Physical and Engineering Sciences*, 366(1884), 4489–4500.
- Fairfield, D., Baumjohann, W., Paschmann, G., Lüher, H., & Sibeck, D. (1990). Upstream pressure variations associated with the bow shock and their effects on the magnetosphere. *Journal of Geophysical Research: Space Physics*, 95(A4), 3773–3786.
- Garcia, K., & Hughes, W. (2007). Finding the lyon-fedder-mobarry magnetopause: A statistical perspective. *Journal of Geophysical Research: Space Physics*, 112(A6).
- Greenstadt, E. W., Green, I. M., Inouye, G. T., Hundhausen, A. J., Bame, S. J., & Strong, I. B. (1968, January). Correlated magnetic field and plasma observations of the Earth's bow shock. *textbackslashjgr*, 73, 51. doi: 10.1029/JA073i001p00051
- Grygorov, K., Šafránková, J., Němeček, Z., Pi, G., Přech, L., & Urbář, J. (2017). Shape of the equatorial magnetopause affected by the radial interplanetary magnetic field. *Planetary and Space Science*, 148, 28–34.
- Gutynska, O., Sibeck, D., & Omid, N. (2015). Magnetosheath plasma structures and their relation to foreshock processes. *Journal of Geophysical Research: Space Physics*, 120(9), 7687–7697.
- Haaland, S., Lybekk, B., Maes, L., Laundal, K., Pedersen, A., Tenfjord, P., ... Snekvik, K. (2017). North-south asymmetries in cold plasma density in the magnetotail lobes: Cluster observations. *Journal of Geophysical Research: Space Physics*, 122(1), 136–149.
- Haaland, S., Reistad, J., Tenfjord, P., Gjerloev, J., Maes, L., DeKeyser, J., ... Dorville, N. (2014). Characteristics of the flank magnetopause: Cluster observations. *Journal of*

- Geophysical Research: Space Physics*, 119(11), 9019–9037.
- Haaland, S., Runov, A., Artemyev, A., & Angelopoulos, V. (2019). Characteristics of the flank magnetopause: Themis observations. *Journal of Geophysical Research: Space Physics*, 124(5), 3421–3435.
- Heikkilä, W. J. (1975). Is there an electrostatic field tangential to the dayside magnetopause and neutral line? *Geophysical Research Letters*, 2(4), 154–157.
- Heikkilä, W. J. (2011). *Earth's Magnetosphere: Formed by the Low-latitude Boundary Layer*. Elsevier.
- Jacobsen, K. S., Phan, T. D., Eastwood, J. P., Sibeck, D. G., Moen, J. I., Angelopoulos, V., ... Fornaçon, K.-H. (2009). THEMIS observations of extreme magnetopause motion caused by a hot flow anomaly. *Journal of Geophysical Research (Space Physics)*, 114, 8210. Retrieved from <http://adsabs.harvard.edu/abs/2009JGRA...114.8210J>
- Jelínek, K., Němeček, Z., Šafránková, J., Shue, J.-H., Suvorova, A. V., & Sibeck, D. G. (2010). Thin magnetosheath as a consequence of the magnetopause deformation: THEMIS observations. *Journal of Geophysical Research (Space Physics)*, 115, 10203. Retrieved from <http://adsabs.harvard.edu/abs/2010JGRA...11510203J>
- Johnson, J. R., Wing, S., & Delamere, P. A. (2014). Kelvin helmholtz instability in planetary magnetospheres. *Space Science Reviews*, 184(1-4), 1–31.
- Karimabadi, H., Krauss-Varban, D., Huba, J., & Vu, H. (2004). On magnetic reconnection regimes and associated three-dimensional asymmetries: Hybrid, hall-less hybrid, and hall-mhd simulations. *Journal of Geophysical Research: Space Physics*, 109(A9).
- Korotova, G. I., Sibeck, D. G., Weatherwax, A., Angelopoulos, V., & Styazhkin, V. (2011). THEMIS observations of a transient event at the magnetopause. *Journal of Geophysical Research (Space Physics)*, 116, 7224. Retrieved from <http://adsabs.harvard.edu/abs/2011JGRA...116.7224K>
- Lindman, E. (1975). “Free-space” boundary conditions for the time dependent wave equation. *J. Comput. Phys.*, 18(1), 66–78.
- Liu, Y.-H., Li, T., Hesse, M., Sun, W., Liu, J., Burch, J., ... Huang, K. (2019). Three-dimensional magnetic reconnection with a spatially confined x-line extent: Implications for dipolarizing flux bundles and the dawn-dusk asymmetry. *Journal of Geophysical Research: Space Physics*, 124(4), 2819–2830.
- Lu, J., Wang, M., Kabin, K., Zhao, J., Liu, Z.-Q., Zhao, M., & Li, G. (2015). Pressure balance across the magnetopause: Global mhd results. *Planetary and Space Science*, 106, 108–115.
- Lu, S., Lin, Y., Angelopoulos, V., Artemyev, A., Pritchett, P., Lu, Q., & Wang, X. (2016). Hall effect control of magnetotail dawn-dusk asymmetry: A three-dimensional global hybrid simulation. *Journal of Geophysical Research: Space Physics*, 121(12), 11–882.
- Luo, H., Chen, G., Du, A., & Xu, W. (2013). Solar wind dependence of energy coupling between solar wind and magnetosphere during intense northward imfs. *Planetary and Space Science*, 79, 82–89.
- Maruca, B. A., Chasapis, A., Gary, S. P., Bandyopadhyay, R., Chhiber, R., Parashar, T., ... others (2018). Mms observations of beta-dependent constraints on ion temperature anisotropy in earth's magnetosheath. *The Astrophysical Journal*, 866(1), 25.
- Masters, A., Slavin, J., DiBraccio, G., Sundberg, T., Winslow, R., Johnson, C., ... Korth, H. (2013). A comparison of magnetic overshoots at the bow shocks of mercury and saturn. *Journal of Geophysical Research: Space Physics*, 118(7), 4381–4390.
- Merka, J., Szabo, A., Šafránková, J., & Němeček, Z. (2003). Earth's bow shock and magnetopause in the case of a field-aligned upstream flow: Observation and model comparison. *Journal of Geophysical Research: Space Physics (1978–2012)*, 108(A7), –.
- Němeček, Z., Šafránková, J., Zastenker, G. N., Pišoft, P., & Jelínek, K. (2002, April). Low-frequency variations of the ion flux in the magnetosheath. *Planetary and Space Science*, 50(5-6), 567–575. doi: 10.1016/S0032-0633(02)00036-3
- Omidi, N., Blanco-Cano, X., Russell, C. T., & Karimabadi, H. (2004, January). Dipolar magnetospheres and their characterization as a function of magnetic moment. *Ad-*

- vances in *Space Research*, 33, 1996–2003. doi: 10.1016/j.asr.2003.08.041
- Palmroth, M., Ganse, U., Pfau-Kempf, Y., Battarbee, M., Turc, L., Brito, T., ... von Althaus, S. (2018, August). Vlasov methods in space physics and astrophysics. *Living Reviews in Computational Astrophysics*, 4(1), 1. doi: 10.1007/s41115-018-0003-2
- Paral, J., & Rankin, R. (2013). Dawn–dusk asymmetry in the kelvin–helmholtz instability at mercury. *Nature Communications*, 4(1), 1–5.
- Parks, G. K. (1991). Physics of space plasmas—an introduction. *Redwood City, CA, Addison-Wesley Publishing Co., 1991, 547 p.*
- Paularena, K., Richardson, J., Kolpak, M., Jackson, C., & Siscoe, G. (2001). A dawn-dusk density asymmetry in earth’s magnetosheath. *Journal of Geophysical Research: Space Physics*, 106(A11), 25377–25394.
- Pi, G., Němeček, Z., Šafránková, J., Grygorov, K., & Shue, J.-H. (2018). Formation of the dayside magnetopause and its boundary layers under the radial imf. *Journal of Geophysical Research: Space Physics*, 123(5), 3533–3547.
- Pi, G., Shue, J.-H., Park, J.-S., Chao, J.-K., Yang, Y.-H., & Lin, C.-H. (2016). A comparison of the imf structure and the magnetic field in the magnetosheath under the radial imf conditions. *Advances in Space Research*, 58(2), 181–187.
- Samsonov, A. (2006). Numerical modelling of the earth’s magnetosheath for different imf orientations. *Advances in Space Research*, 38(8), 1652–1656.
- Samsonov, A., Bogdanova, Y., Branduardi-Raymont, G., Sibeck, D., & Toth, G. (2020). Is the relation between the solar wind dynamic pressure and the magnetopause standoff distance so straightforward? *Geophysical Research Letters*, 47(8), e2019GL086474.
- Samsonov, A., Sibeck, D., Šafránková, J., Němeček, Z., & Shue, J.-H. (2017). A method to predict magnetopause expansion in radial imf events by mhd simulations. *Journal of Geophysical Research: Space Physics*, 122(3), 3110–3126.
- Samsonov, A. A. (2011, January). Propagation of inclined interplanetary shock through the magnetosheath. *Journal of Atmospheric and Solar-Terrestrial Physics*, 73, 30–39. doi: 10.1016/j.jastp.2009.10.014
- Samsonov, A. A., & Pudovkin, M. I. (2000, June). Application of the bounded anisotropy model for the dayside magnetosheath. *Jgr*, 105, 12859–12868. doi: 10.1029/2000JA900009
- Shue, J.-H., Chao, J.-K., Song, P., McFadden, J., Suvorova, A., Angelopoulos, V., ... Plaschke, F. (2009). Anomalous magnetosheath flows and distorted subsolar magnetopause for radial interplanetary magnetic fields. *Geophysical Research Letters*, 36(18).
- Sibeck, D. G., Allen, R., Aryan, H., Bodewits, D., Brandt, P., Branduardi-Raymont, G., ... others (2018). Imaging plasma density structures in the soft x-rays generated by solar wind charge exchange with neutrals. *Space Science Reviews*, 214(4), 79.
- Sibeck, D. G., Decker, R. B., Mitchell, D. G., Lazarus, A. J., Lepping, R. P., & Szabo, A. (2001). Solar wind preconditioning in the flank foreshock: IMP 8 observations. *J. Geophys. Res.*, 106, 21675–21688. Retrieved from <http://adsabs.harvard.edu/abs/2001JGR...10621675S>
- Sibeck, D. G., Kudela, K., Lepping, R. P., Lin, R., Nemecek, Z., Nozdachev, M. N., ... Yermolaev, Y. (2000). Magnetopause motion driven by interplanetary magnetic field variations. *J. Geophys. Res.*, 105, 25155–25170. Retrieved from <http://adsabs.harvard.edu/abs/2000JGR...10525155S>
- Sorathia, K., Merkin, V., Ukhorskiy, A., Allen, R., Nykyri, K., & Wing, S. (2019). Solar wind ion entry into the magnetosphere during northward imf. *Journal of Geophysical Research: Space Physics*, 124(7), 5461–5481.
- Spreiter, J. R., & Alksne, A. Y. (1969). Plasma flow around the magnetosphere. *Reviews of Geophysics*, 7(1-2), 11–50.
- Spreiter, J. R., & Stahara, S. S. (1984). *Magnetohydrodynamic and gasdynamic theories for planetary bow waves*. Wiley Online Library.
- Suvorova, A., & Dmitriev, A. (2015). Magnetopause inflation under radial imf: Comparison of models. *Earth and Space Science*, 2(4), 107–114.

- Suvorova, A. V., Shue, J.-H., Dmitriev, A. V., Sibeck, D. G., McFadden, J. P., Hasegawa, H., ... Němeček, Z. (2010). Magnetopause expansions for quasi-radial interplanetary magnetic field: THEMIS and Geotail observations. *Journal of Geophysical Research (Space Physics)*, *115*, 10216. Retrieved from <http://adsabs.harvard.edu/abs/2010JGRA...11510216S>
- Tan, B., Lin, Y., Perez, J., & Wang, X. (2011). Global-scale hybrid simulation of dayside magnetic reconnection under southward imf: Structure and evolution of reconnection. *Journal of Geophysical Research: Space Physics*, *116*(A2).
- Treumann, R. (2009). Fundamentals of collisionless shocks for astrophysical application, 1. Non-relativistic shocks. *The Astronomy and Astrophysics Review*, *17*(4), 409–535.
- Turc, L., Tardus, V., Dimmock, A., Battarbee, M., Ganse, U., Johlander, A., ... Palmroth, M. (2020). Asymmetries in the earth's dayside magnetosheath: results from global hybrid-vlasov simulations. *Annales Geophysicae Discussions*, *2020*, 1–24. Retrieved from <https://www.ann-geophys-discuss.net/angeo-2020-13/> doi: 10.5194/angeo-2020-13
- Turner, D., Wilson, L., Liu, T., Cohen, I., Schwartz, S., Osmane, A., ... others (2018). Autogenous and efficient acceleration of energetic ions upstream of earth's bow shock. *Nature*, *561*(7722), 206–210.
- Vafin, S., Riazantseva, M., & Pohl, M. (2019). Coulomb collisions as a candidate for temperature anisotropy constraints in the solar wind. *The Astrophysical Journal Letters*, *871*(1), L11.
- Villasenor, J., & Buneman, O. (1992). Rigorous charge conservation for local electromagnetic field solvers. *Comput. Phys. Commun.*, *69*(2), 306–316.
- Šafránková, J., Němeček, Z., Santolík, O., Sibeck, D. G., Zastenker, G. N., & Skalsky, A. (2000). The Flank Magnetopause: Interball Observations. *Advances in Space Research*, *25*, 1503–1510. Retrieved from <http://adsabs.harvard.edu/abs/2000AdSpR...25.1503S>
- Walsh, A. P., Haaland, S., Forsyth, C., Keesee, A. M., Kissinger, J., Li, K., ... Taylor, M. G. G. T. (2014, July). Dawn-dusk asymmetries in the coupled solar wind-magnetosphere-ionosphere system: a review. *Annales Geophysicae*, *32*, 705–737. Retrieved from <https://ui.adsabs.harvard.edu/abs/2014AnGeo...32..705W> doi: 10.5194/angeo-32-705-2014
- Walsh, B. M. (2017). Magnetopause plasma parameters and asymmetries in solar wind-magnetosphere coupling. *Dawn-Dusk Asymmetries in Planetary Plasma Environments*, 29–39.
- Walsh, B. M., Sibeck, D. G., Wang, Y., & Fairfield, D. H. (2012). Dawn-dusk asymmetries in the Earth's magnetosheath. *Journal of Geophysical Research (Space Physics)*, *117*, 12211. Retrieved from <http://adsabs.harvard.edu/abs/2012JGRA...11712211W>
- Wang, C.-P., Lyons, L. R., Weygand, J. M., Nagai, T., & McEntire, R. W. (2006). Equatorial distributions of the plasma sheet ions, their electric and magnetic drifts, and magnetic fields under different interplanetary magnetic field b_z conditions. *Journal of Geophysical Research: Space Physics*, *111*(A4).
- Wang, J., Guo, Z., Yasong, S. G., Du, A., Huang, C., & Qin, P. (2018). The responses of the earth's magnetopause and bow shock to the imf b_z and the solar wind dynamic pressure: a parametric study using the amr-cese-mhd model. *Journal of Space Weather and Space Climate*, *8*, A41.
- Willis, D. (1978). The magnetopause: Microstructure and interaction with magnetospheric plasma. *Journal of Atmospheric and Terrestrial Physics*, *40*(3), 301–322.
- Yu, Y., & Ridley, A. J. (2009, December). The response of the magnetosphere-ionosphere system to a sudden dynamic pressure enhancement under southward IMF conditions. *Annales Geophysicae*, *27*(12), 4391–4407. doi: 10.5194/angeo-27-4391-2009
- Zhang, H., Fu, S., Pu, Z., Lu, J., Zhong, J., Zhu, C., ... Liu, L. (2019, aug). Statistics on the magnetosheath properties related to magnetopause magnetic reconnection. *The Astrophysical Journal*, *880*(2), 122. Retrieved from <https://doi.org/10.3847/1538-4357/ab290e> doi: 10.3847/1538-4357/ab290e

1205

8 Figures

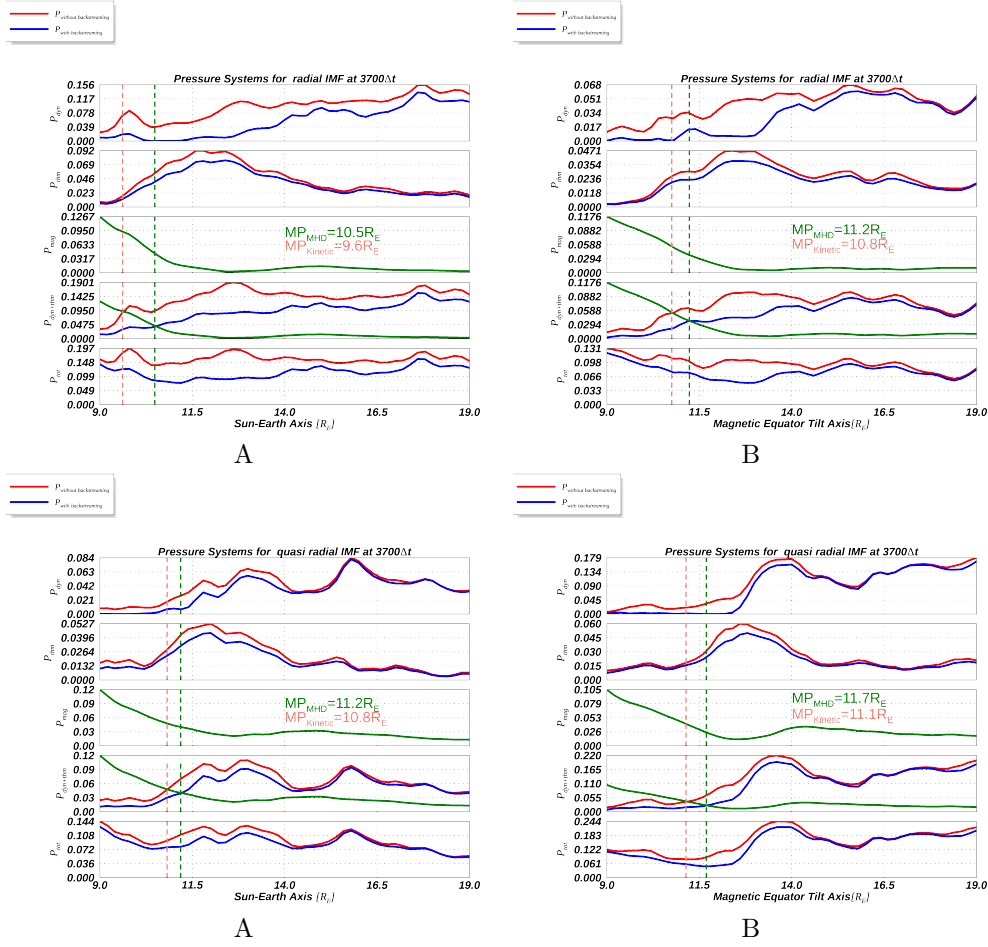


Figure 2. This Figure shows the pressure systems (dynamic, thermal and magnetic) for both IMF orientations plotted in spherical coordinates at two locations ($\phi = -180^\circ$ and $\theta = 0, 31^\circ$). Kinetic effects are plotted in blue, and the removal of backstreaming ions are plotted in red, so that the kinetic effect appears by the difference of the impact of bulk and the absence of backstreaming SW ions. Measurements without accounting for backstreaming (no kinetic effect) results in compressing the MP earthward. MP sizes read $10.5, 9.7 R_E$ with and without backstreaming ions along Sun-Earth Line and $11.2, 10.8 R_E$ along tilted magnetic equator axis for radial IMF. While same values for quasi-radial IMF are $11.2, 10.8 R_E$ and $11.7, 11.1 R_E$, respectively.

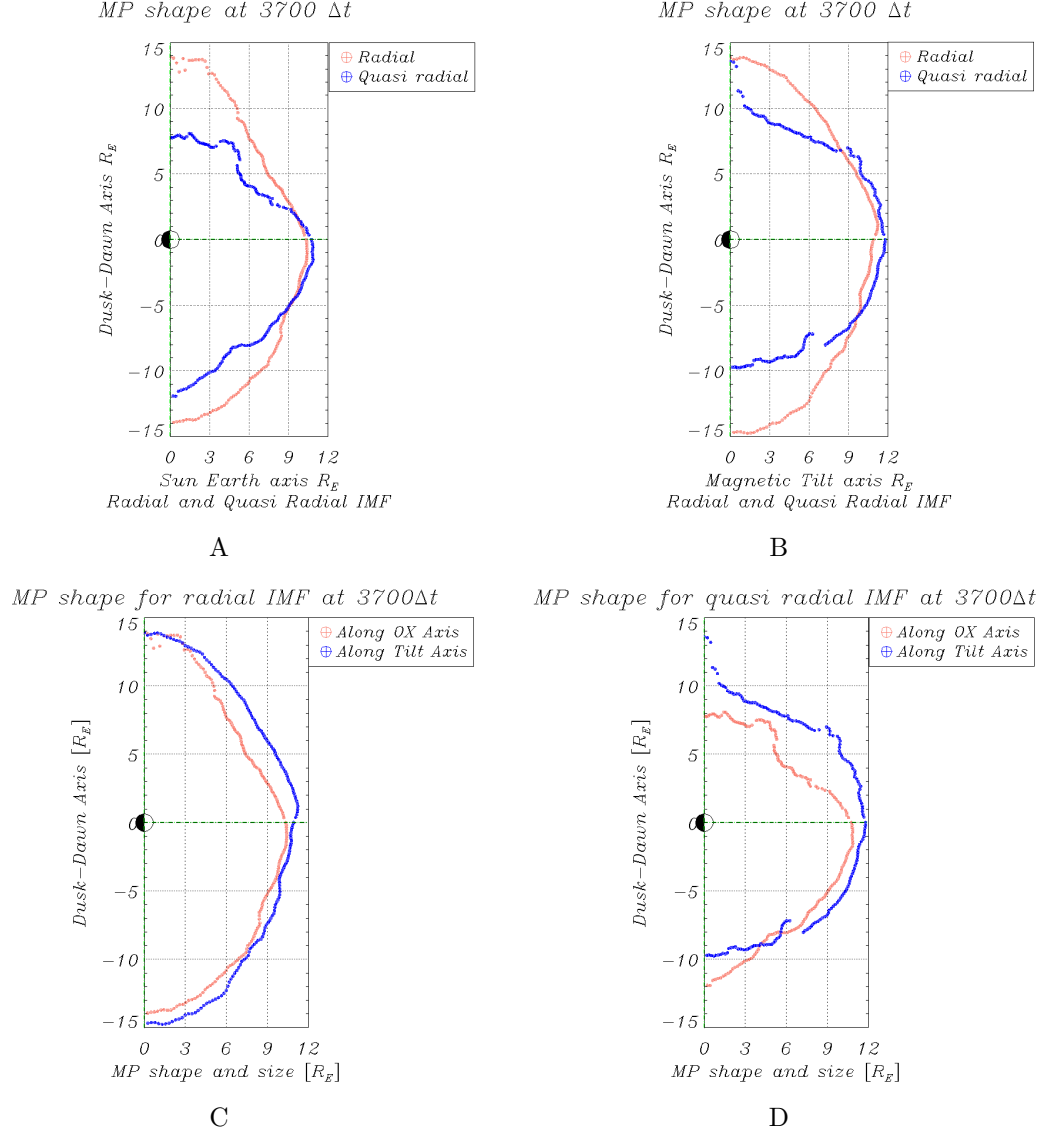


Figure 3. This figure shows the comparison between the MP shape for radial and quasi-radial IMF (panel A&B) and the MP shape for same IMF orientation but taken along sun-earth line and the tilted magnetic equator axis (panel C&D). All plots are in the equatorial plane. The MP shapes are calculated in the planes defined by $\theta=0^\circ$ & -31° , respectively (each fixed θ value defines a unique plane in which the MP size is measured).

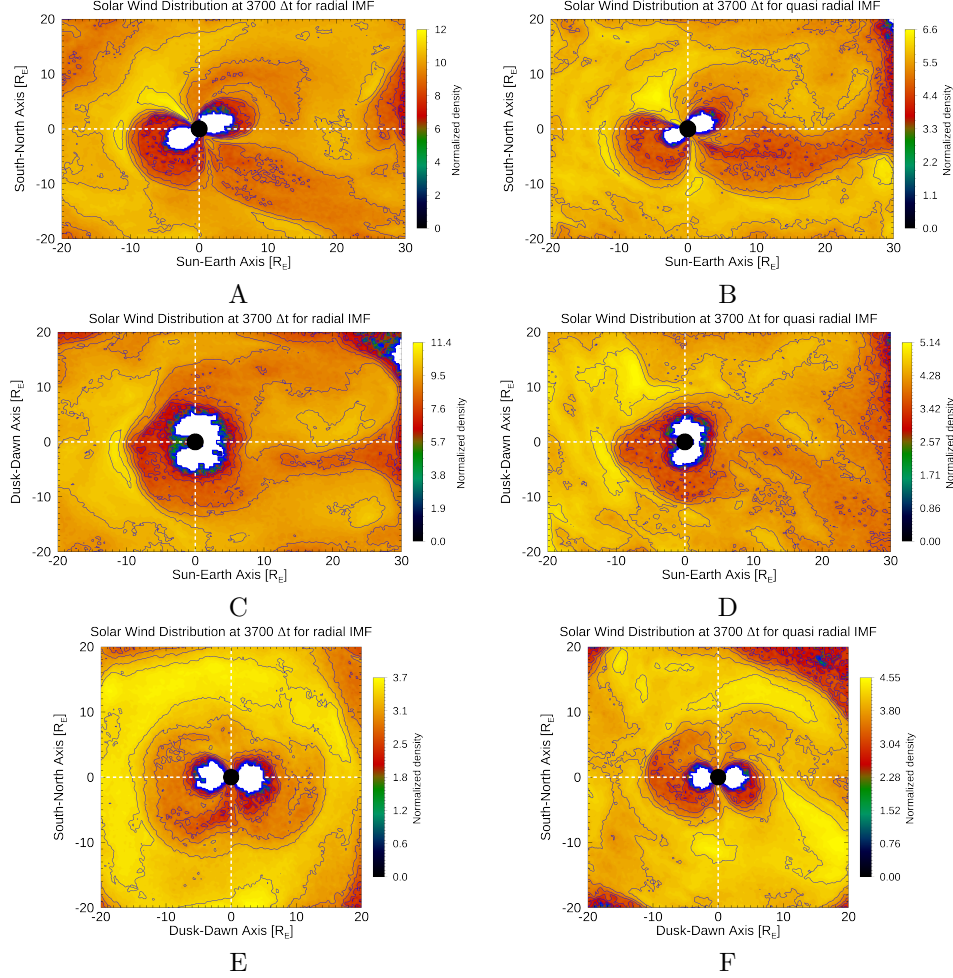


Figure 4. This figure shows data plots for radial IMF. Contour density plasma distribution plots are shown in panels, A, C, and E for radial IMF and their corresponding density plots are shown in panels, B, D, and F for quasi-radial IMF. In panel A, 2D plasma distribution in XZ plane, shows dipole tilt and the SW plasma complex structure at the magnetosheath. High density cap-like structure covers the high latitude MP until it hits the northern cusp. This structure is due to dipole tilt effect and it is smaller in size for quasi-radial case shown in panel B. The equatorial plane plasma distribution is complex with different contour structure and densities in panels C & D. While the asymmetric structure of plasma distribution in dusk-dawn structure, panels E & F clearly shows the complexity of the system in the above panels.

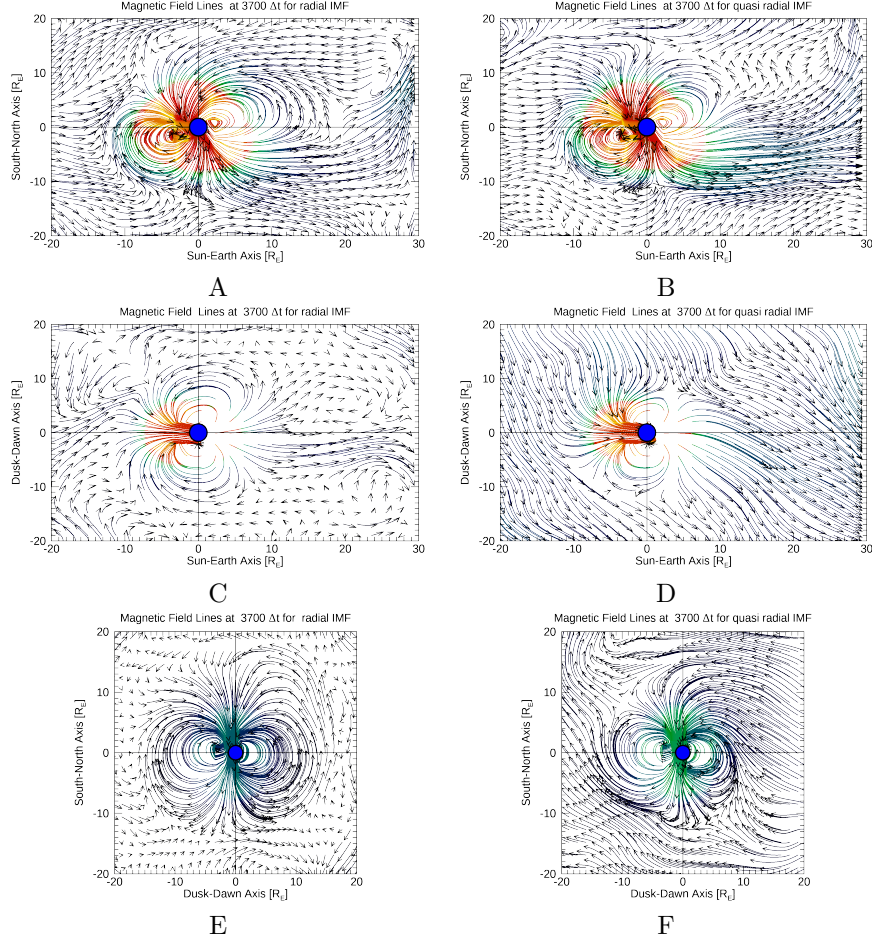


Figure 5. This figure shows the corresponding magnetic field lines of (Fig.4), In panel A, C, and E, radial and B, D, and F quasi radial IMF, taken at step time 3700 Δt in XZ plane($x=-20,30,z=-20,20$) R_E , XY-plane($x=-20,30,y=-20,20$) R_E , YZ-plane($y=-20,20,z=-20,20$) R_E . This large scale field topology shows the potential reconnection sights, open/close field lines which explain the plasma distribution in the corresponding panels for both IMF orientations.

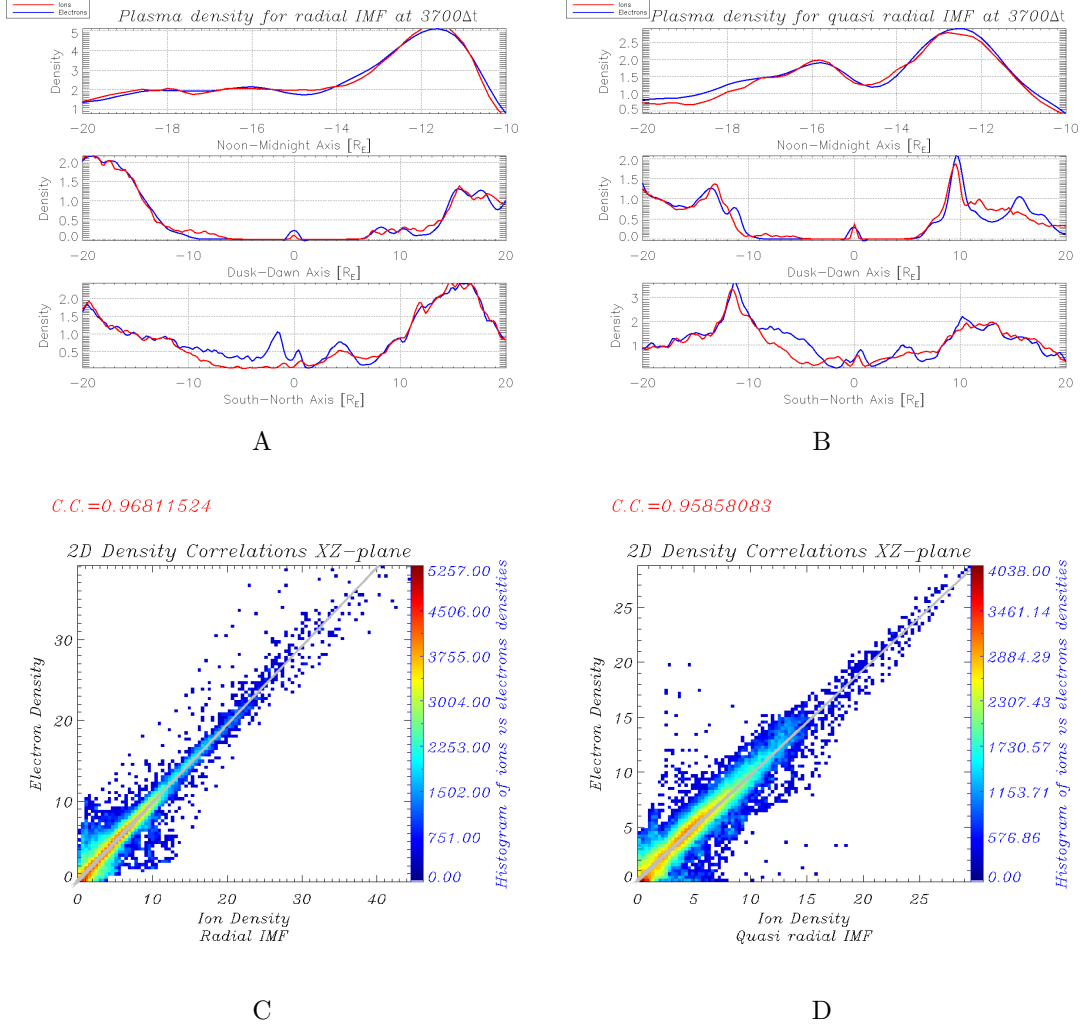


Figure 6. Ion and electron densities are plotted in 3D, along OX($Y=Z=0$), OY($X=Z=0$), and OZ($X=Y=0$) for radial IMF in panel A and for quasi-radial IMF in panel B. Their values are normalized to the initial density. The density profile is plotted only in the dayside magnetosphere. Scatter plot for ions and electrons density in 2D is shown in panels, C&D. It is found that the correlation coefficients (C.C.) equal to (0.97, 0.96) for radial and quasi-radial IMF, respectively. Values are averaged over $2R_E$ in Y.

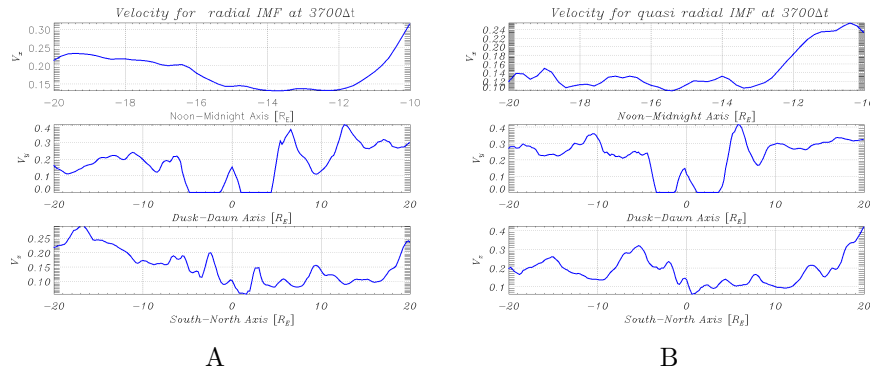


Figure 7. Ion velocity modulus for both IMF orientation are plotted in 3D as in Fig. 6

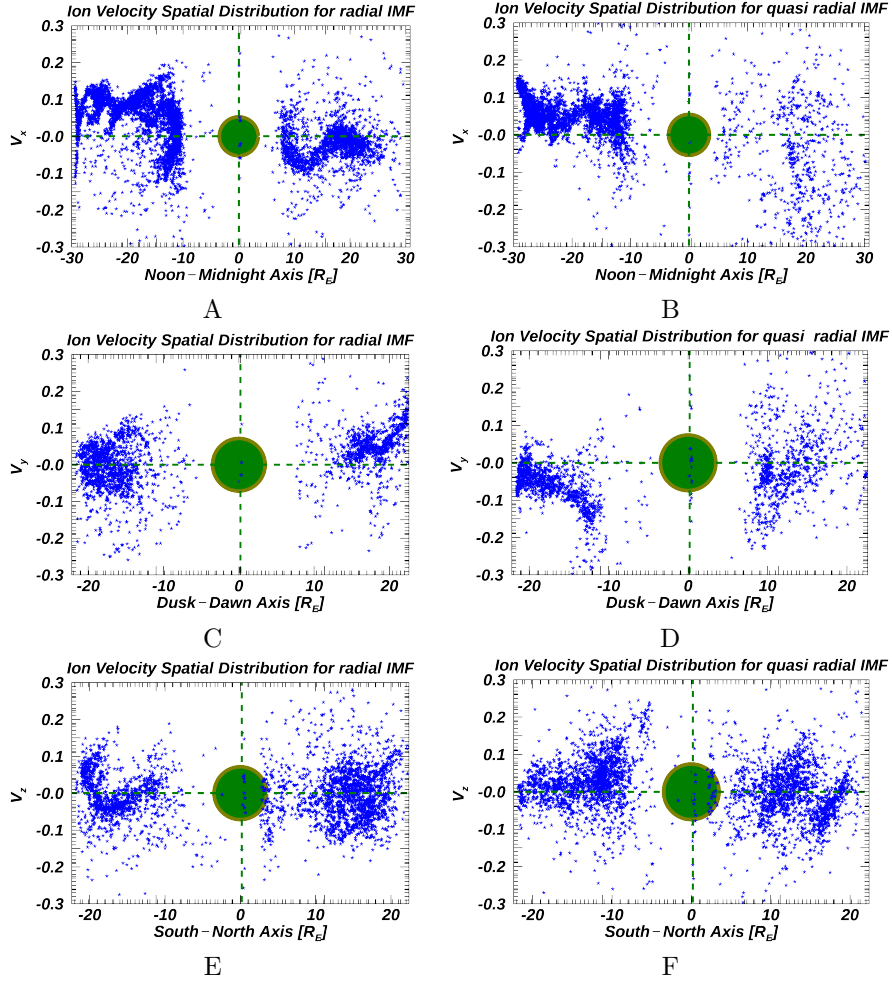


Figure 8. Full range slices for ions velocity spatial distribution measured at the planet position in 3D. In panel A and B, V_x is plotted at $y=z=0$ for radial and quasi-radial IMF. Similarly in panel C and D, V_y is plotted at $x=z=0$ and in panel E and F, V_z is plotted at $x=y=0$ respectively.

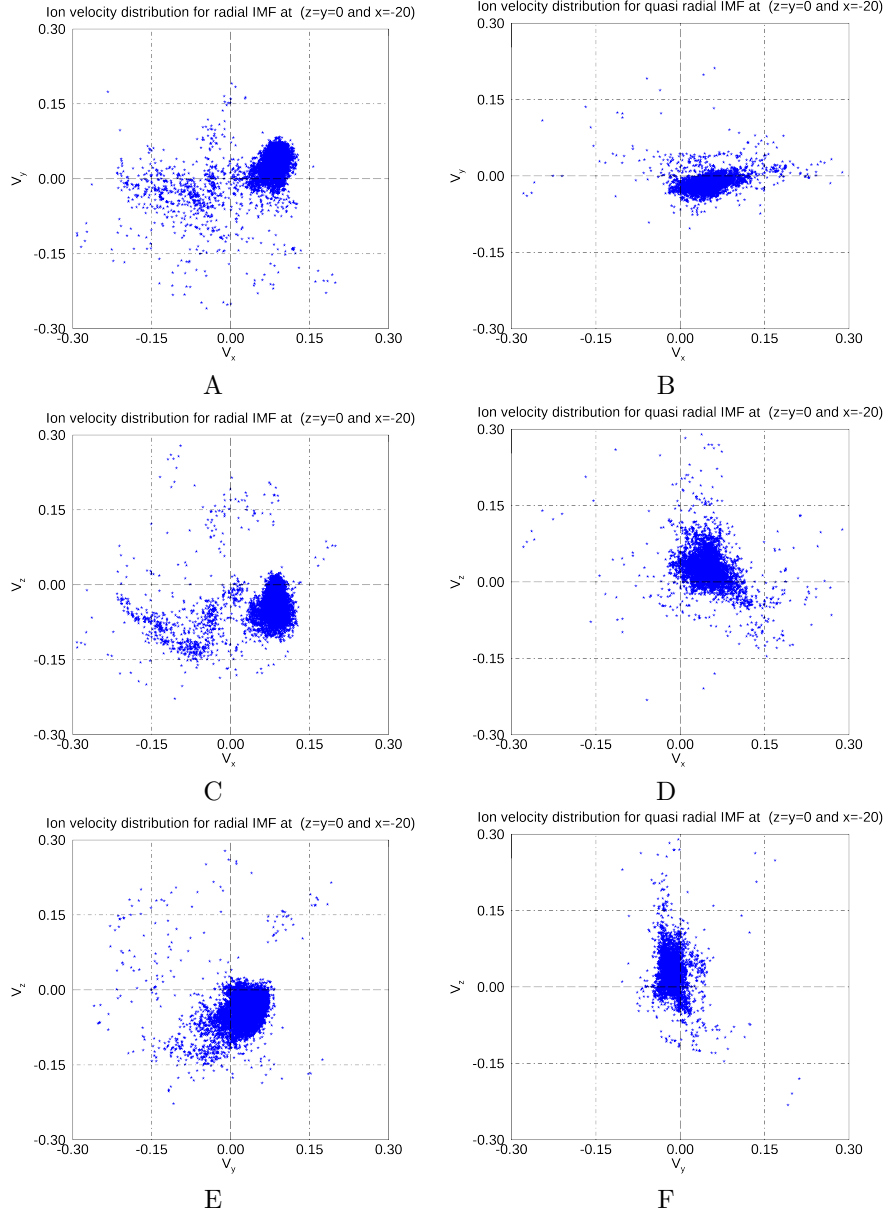


Figure 9. This figure shows the ion velocity distribution measured at $-20R_E$ in the dayside magnetosphere to track particle backstreaming (kinetic effect) ahead of the foreshock region. In panel A, there is a substantial ratio of gyrating ions for radial IMF but not for quasi-radial IMF (panel B) in XY plane taken at the planet position ($z=y=0$). Again, in panel E and F the backstreaming ions in XZ plane appear larger for radial than quasi-radial IMF and it is the case for YZ plane as well.

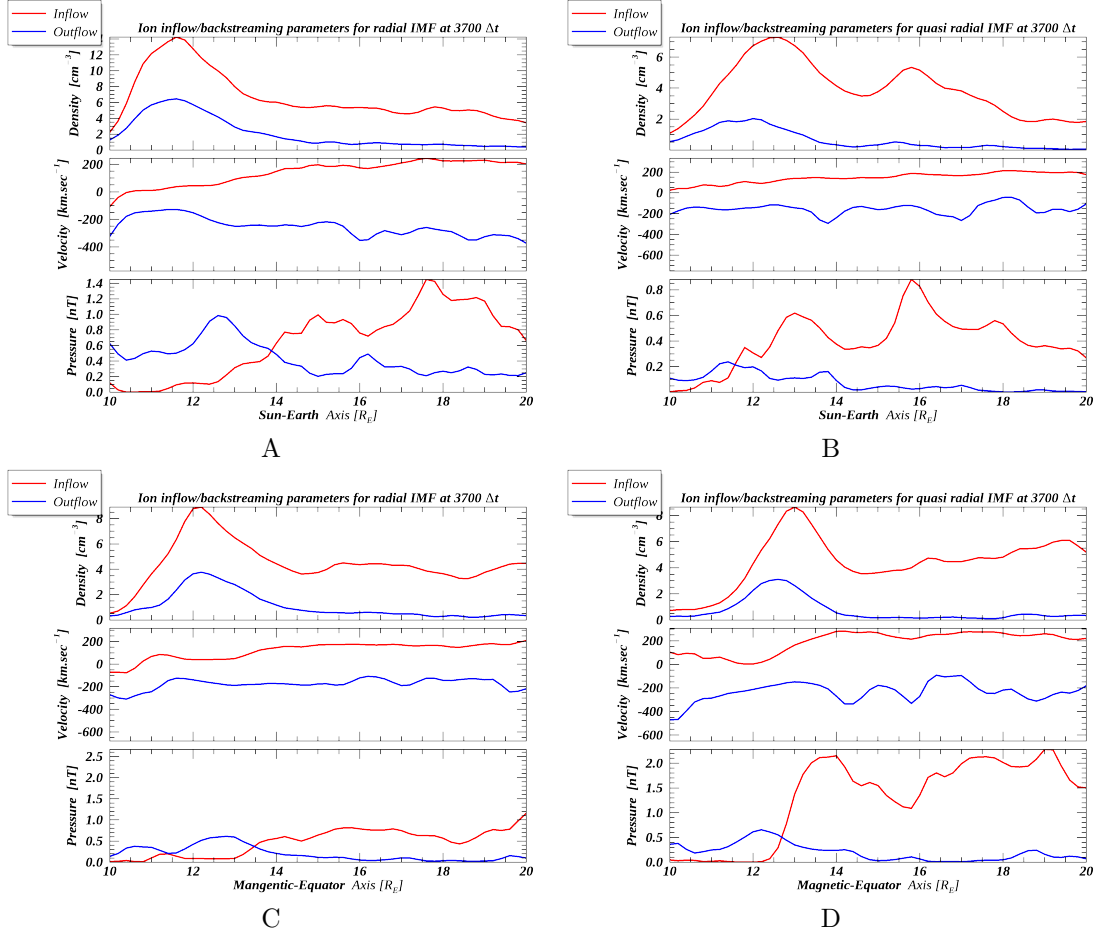


Figure 10. This figure shows the inflow/backstreaming SW ions density, velocity and dynamic pressure calculated in spherical coordinates for both IMF orientations at two locations, namely along Sun-Earth axis and tilted magnetic equator. The backstreaming ions are plotted in (blue) and the inflow ions are plotted in (red). The backstreaming ions are larger in radial IMF than quasi-radial IMF (see velocity distribution function in Fig. 9). The four plots confirm the fact that velocity and density contribute differently in the dynamic pressure, same results in the recent study of (A. Samsonov et al., 2020).

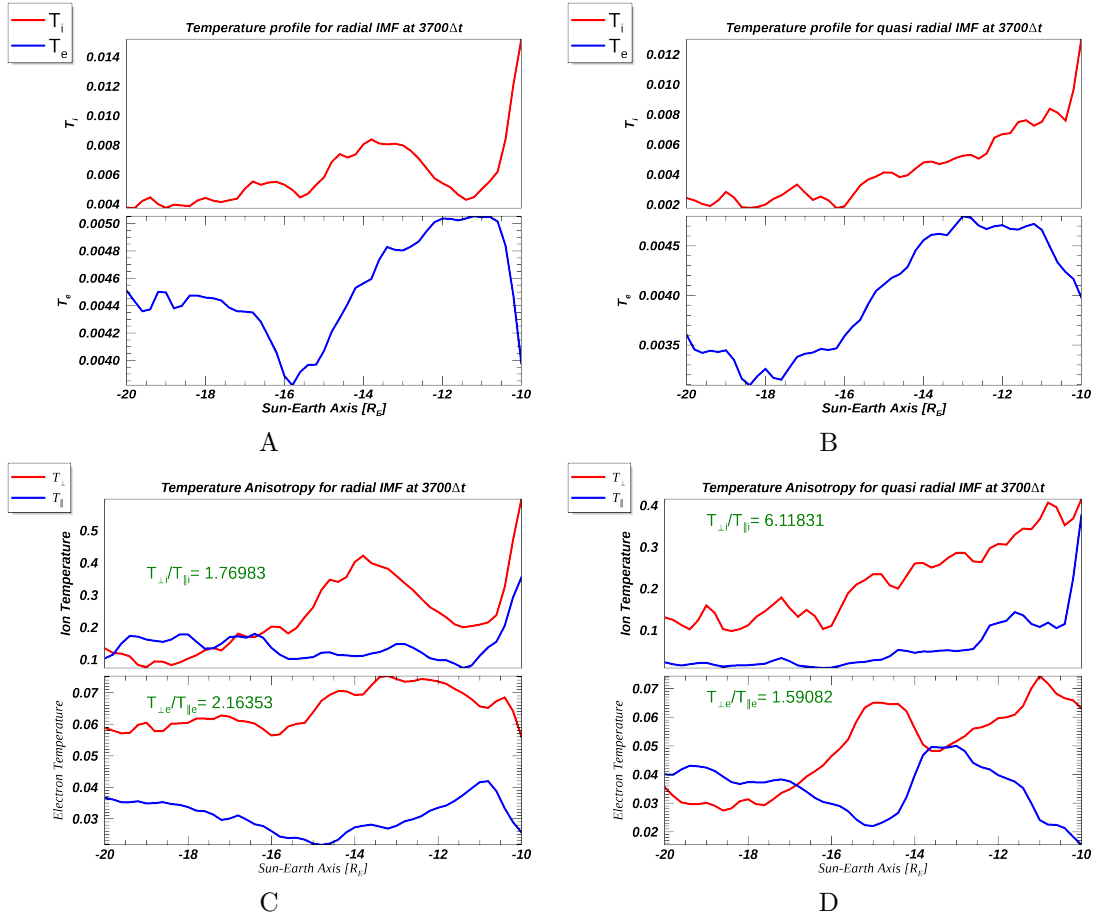


Figure 11. This figure shows ion and electron temperatures for both IMF orientations. In Panel A, $T_i \approx 1.5T_e$ in the magnetosheath. For purely radial IMF, after increasing just after the shock, T_i is found decreasing in the magnetosheath until it jumps again inside the magnetosphere. T_e also increases after the shock and remains almost constant in the magnetosheath before decreasing inside the magnetosphere. In panel B for quasi-radial IMF, the ratio $T_i/T_e \approx 1.13$, and T_i is constantly increasing in the magnetosheath, and jumps at the magnetospheric boundary of the MP. T_e has almost the same behavior as for the radial case. In panels C and D, temperature anisotropy is plotted as in A & B. The $T_{\perp i}/T_{\parallel i}$ is ≈ 1.8 for radial IMF and 6 for quasi-radial IMF. Whilst this ratio for electrons ($T_{\perp e}/T_{\parallel e}$) reads 2.2 times for radial IMF and 1.6 times for quasi-radial. The $(T_{\perp i}/T_{\parallel i})$ correlation coefficients (C.C.) are (0.23, 0.8) for radial and quasi-radial IMF, respectively, while the corresponding $(T_{\perp e}/T_{\parallel e})$ C.C. for electrons shows anti correlations of (-0.07, -0.5).

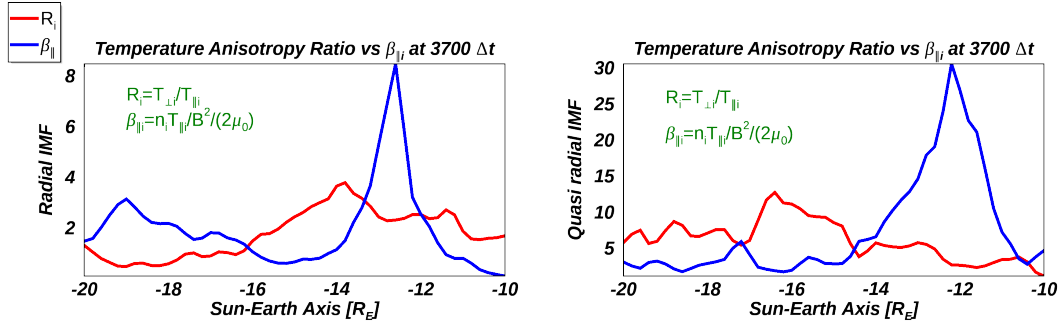


Figure 12. Left panel, the ion temperature anisotropy ratio R_i (defined on the plot) is plotted versus parallel beta ($\beta_{||}$) for radial IMF, next to the right same figure is plotted for quasi-radial IMF. The average $\beta_{||} = (2, 7)$ for radial and quasi-radial IMF, respectively.

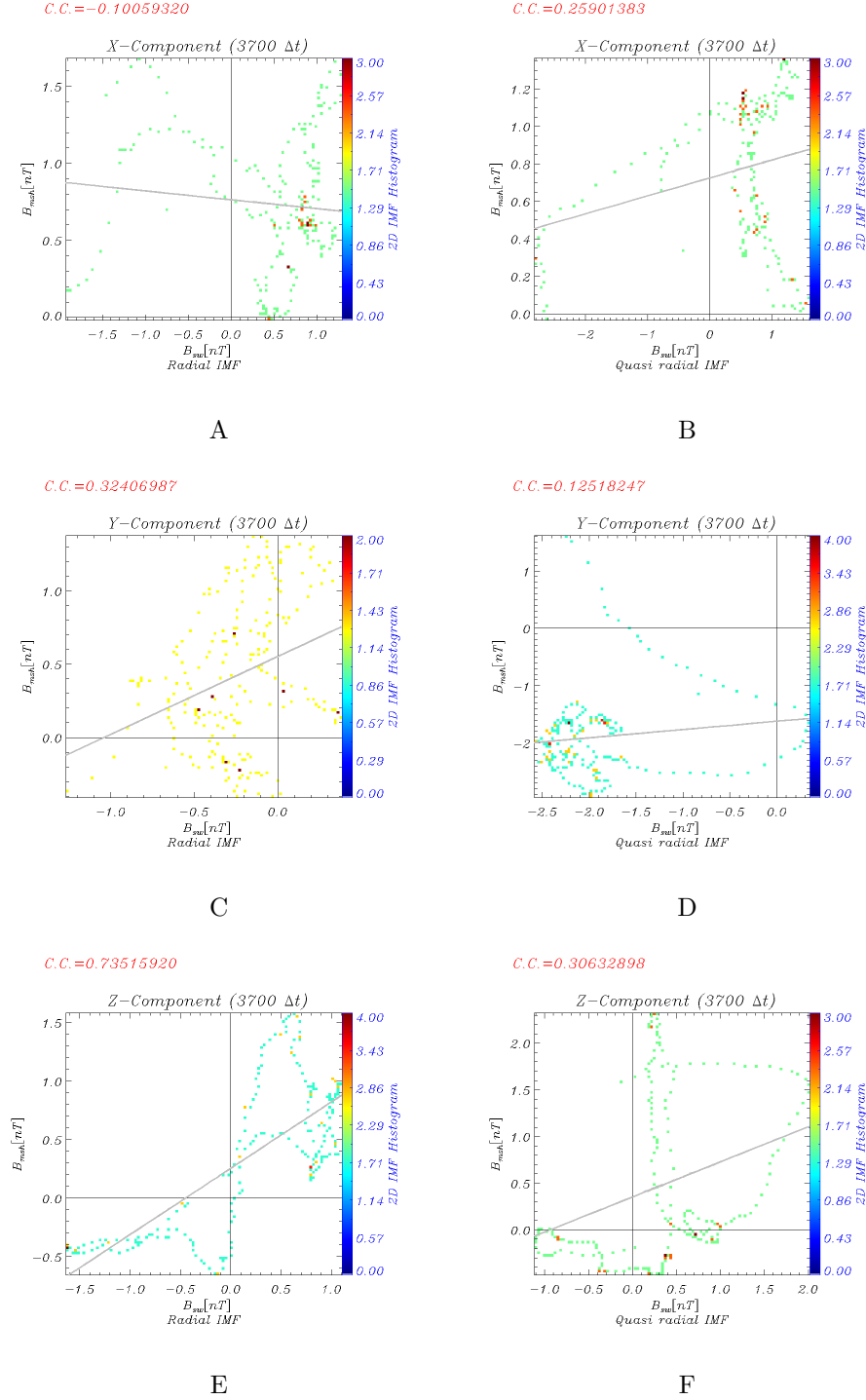


Figure 13. This Figure shows the scatter plots of magnetic field in 3D for two IMF orientations and measured in the SW at $\approx 20R_E$ and in the magnetosheath at $\approx 12R_E$. The correlation coefficient (C.C) is measured for radial and quasi-radial IMF. The best C.C. (0.74) is found for purely radial IMF in Z-component between the magnetic fields in the aforementioned regions while in X-component it is found the poorest with negative value(-0.1) for radial IMF, but for quasi-radial IMF the X-component C.C. is 0.25. On contrary X & Z-component of the C.C. for quasi-radial IMF shows closest values i.e. (0.26,0.30)

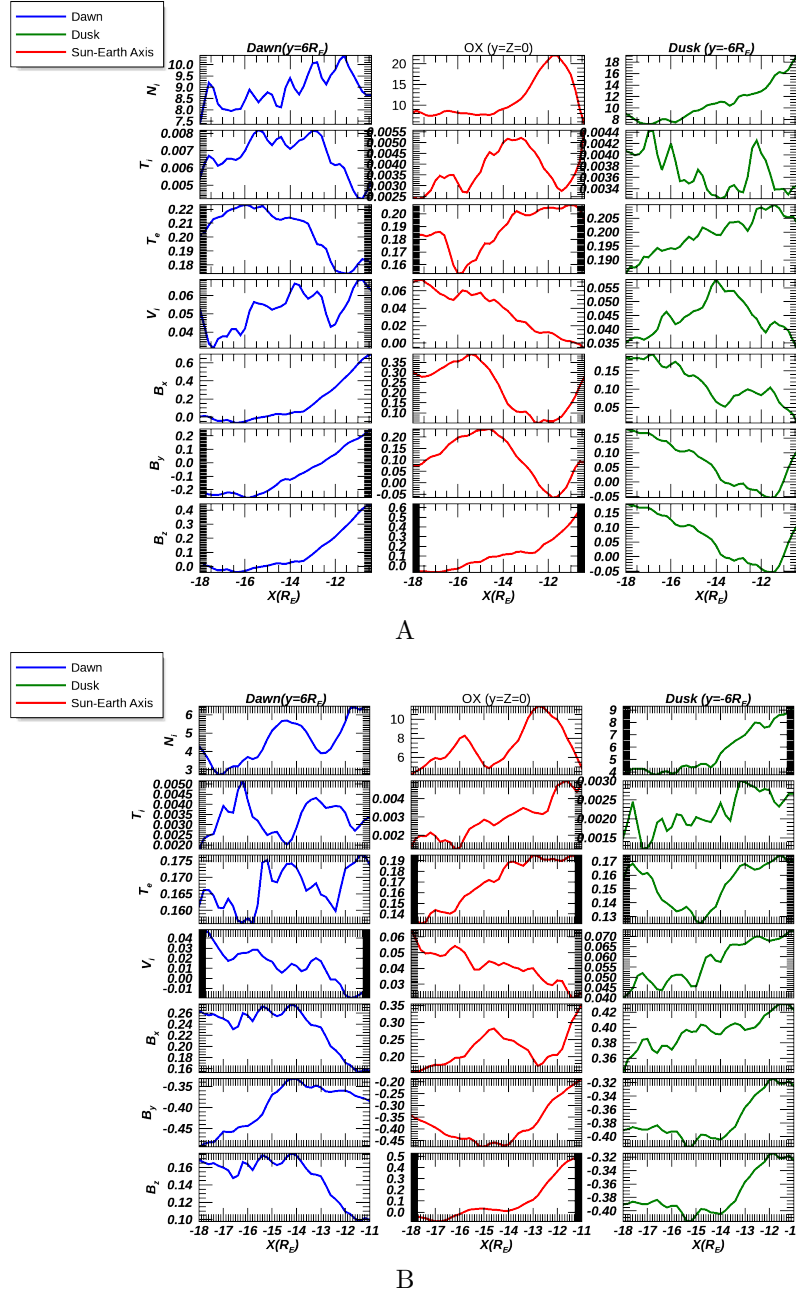


Figure 14. Plasma parameters N_i , T_i , T_e , V_i , B_x , B_y and B_z are plotted along all the X-direction of the simulation box (≈ -18 to $-10R_E$) for radial IMF (panel A) and quasi-radial IMF (panel B). The color code in the figure is such that dusk (green), dawn (blue) and along OX (red). For all parameters, all quantities show dawn-dusk asymmetries. Quantified values of solar wind parameters at the derived MP position is shown in Tables 8 and 9